

1 **Combined genomic and imaging techniques show intense arsenic enrichment caused**
2 **by detoxification in a microbial mat of the Dead Sea shore**

3 **C. Thomas^{1*}, M. Filella², D. Ionescu³, S. Sorieul⁴, C. G. L. Pollier⁵, A. M. Oehlert⁵, P.**
4 **Zahajská⁶, N. Gedulter⁷, A. Agnon⁷, D. Ferreira Sanchez⁸, and D. Ariztegui¹**

5 ¹ Department of Earth Sciences, University of Geneva, Geneva, Switzerland.

6 ² Department F.-A. Forel, University of Geneva, Geneva, Switzerland.

7 ³ Leibniz Institute for Freshwater Ecology and Inland Fisheries, Stechlin, Germany.

8 ⁴ CNRS, University of Bordeaux, LP2iB, Gradignan, France.

9 ⁵ Rosenstiel School of Marine, Atmospheric, and Earth Science, University of Miami, Miami,
10 USA.

11 ⁶ Institute of Geography & Oeschger Centre for Climate Change Research, University of Bern,
12 Bern, Switzerland.

13 ⁷ Hebrew University of Jerusalem, Institute of Earth Sciences, Jerusalem, Israel.

14 ⁸ Swiss Light Source, Paul Scherrer Institute, Villigen, Switzerland.

15
16 Corresponding author: Camille Thomas (camille.thomas@unibe.ch)

17
18 * Current affiliation: Institute of Geological Sciences and Oeschger Centre for Climate Research,
19 University of Bern, Bern, Switzerland

20
21 **Key Points:**

- 22 • Intense arsenic enrichment is detected for the first time around the Dead Sea
23 • Arsenic is accumulated in the organic matter of a microbial mat as methylated
24 organoarsenic
25 • The enrichment results from microbial detoxification and may be fossilized
26

27 **Abstract**

28 Microbial mats and microbialites are essential tools for reconstructing early life and its
29 environments. To better understand microbial trace element cycling, a microbial mat was
30 collected from the sinkhole systems of the western shores of the Dead Sea, a dynamic
31 environment exhibiting diverse extreme environments. Intense arsenic enrichment was measured
32 (up to 6.5 million times higher than current concentrations in water, and 400 times the bulk
33 concentration in the mat). Arsenic was found predominantly as As(V) in organic molecules, as
34 shown by XANES spectra and high-resolution elemental mapping. Arsenic cycling genes
35 obtained from metagenomic analysis were associated with arsenic detoxification, supporting an
36 active mechanism of As(V) uptake, As(III) efflux and organoarsenic accumulation in the
37 extracellular polymeric substances of the mat. Thus, we propose that such localized As
38 enrichment can be attributed to a transient increase in As(V) concentrations in the circulating
39 subsurface water of the Dead Sea shore and its subsequent incorporation into organoarsenic
40 molecules through microbial detoxification processes.

41
42 Our dataset supports the possibility of metalloid enrichments recorded in very localized facies
43 due to rapid geogenic fluctuations in chemistry of the water flowing over a biofilm. In this
44 context, this example calls for caution in interpreting metal(loid) enrichment in organic matter-
45 rich layers and microbialites of Paleoproterozoic origins. Arsenic signatures in Precambrian
46 organic matter and carbonate rocks may host biosignatures, including evidence for extracellular
47 polymeric substances, As-binding and detoxification processes, without supporting arsenotrophy.
48 They do, however, provide clues to better assess the paleoenvironmental conditions at the time of
49 microbial mat formation.

50 **Plain Language Summary**

51 Microbial mats and microbialites are like time machines helping us learn about ancient life and
52 its environments. We collected a microbial mat from the unique Dead Sea's sinkholes, where life
53 thrives in extreme conditions. In this mat, we found for the first time in this area a staggering 6.5
54 million-fold increase in arsenic, an element toxic to life. By closely studying the genes and
55 chemistry of this microbial mat, we discovered that microbes were striving to clean up this
56 excess arsenic, in a sort of natural detoxification process. It seems that a temporary spike in
57 arsenic levels in the Dead Sea water triggered this clean-up work, which eventually stored the
58 arsenic safely in the mat, away from the microbial cells. Our findings suggest that in the past,
59 when microbial mats were one of the only ecosystems on Earth, changes in the water flowing
60 over mats like this one could have caused similar accumulations of metals. So, when scientists
61 study ancient fossilized microbial layers, these discoveries can help us look into the past and
62 understand the chemical and biological conditions under which these ancient microbial mats
63 formed.

64

65

66 **1 Introduction**

67 Despite its low abundance in the Earth's crust, arsenic (As) is a common element in the
68 environment. It is known for its toxicity to life, mainly because of the use of As₂O₃ for murders
69 by poisoning. What is true for humans is also true for the rest of the tree of life. For example, the
70 common form of As in the environment, arsenate -As(V)- is molecularly close to phosphate and
71 can enter microbial cells via phosphate transporters and inhibit oxidative phosphorylation.
72 Several mechanisms have evolved to cope with and remove As from cells. They generally
73 involve arsenate -As(V)- reduction to arsenite -As(III)- and expulsion pathways through the *Ars*
74 operon, involving the transport of arsenite and/or methylation reactions into less and non-toxic
75 organic molecules (Rosen, 2002; Xu et al., 1998). Some examples found in the environment are
76 methylarsonate, dimethylarsinate, mono and dimethylarsinic acid, trimethylarsine oxide,
77 tetramethylarsonium or volatile trimethylarsine (Honschopp et al., 1996; Lakso & Peoples, 1975;
78 McBride & Wolfe, 1971; Zhu et al., 2014), arsenobetaine (the only non-toxic organoarsenic;
79 Caumette et al., 2012; Edmonds et al., 1977), or arseno-sugars (Morita & Shibata, 1990). In this
80 context, life plays an important role in global As cycling through the employment of such
81 detoxification processes. Additionally, some prokaryotes also use As(V) as their respiratory
82 oxidant coupled to organic matter oxidation (Oremland & Stolz, 2003). These dissimilatory
83 arsenate-reducing organisms include *Proteobacteria*, *Firmicutes*, *Clostridia*, and thermophilic
84 *Archaea* isolated from freshwater sediments, soda lakes, hot springs (Oremland & Stolz, 2003),
85 aquifers (Saikat et al., 2001) or animal digestive tracts (Herbel et al., 2002). They all use an
86 arsenate respiratory reductase (*arr*) thought to have evolved from the polysulfide reductase
87 enzyme allowing respiratory conversion of S⁰ to H₂S (Duval et al., 2008). Heterotrophic and
88 chemolithoautotrophic arsenite oxidizers can also cycle arsenite as a detoxification system using
89 the *aio* enzyme (Anderson et al., 1992) or through the use of As(III) as electron donor for nitrate
90 reduction (Zargar et al., 2010) or anoxygenic photosynthesis (Kulp et al., 2008) via the *arxA*
91 gene found in *Gammaproteobacteria Thioalkalivibrio* and *Halomonas* for example (Edwardson
92 & Hollibaugh, 2017). *ArxA*, *aioA*, *arrA* all belong to the Dimethylsulfoxide (DMSO) reductase
93 superfamily of molybdenum-containing enzymes (Andres & Bertin, 2016; McEwan et al., 2002).
94 Arsenite oxidase (*aio*) has been suggested to emerge before the Archaea/Bacteria divide (Lebrun
95 et al., 2003), inferring the presence and role of arsenite in biogeochemical cycling of Archean
96 habitats (Mukhopadhyay et al., 2002; Sforza et al., 2014), along with mechanisms to cope with
97 its toxicity (Chen et al., 2020). Respiratory arsenate reductase (*arrA*), and the arsenate resistance
98 system is suggested to have evolved contemporaneously with the oxygenation of the atmosphere
99 (Duval et al., 2008), in concert with increased photosynthetic activity around the Great Oxidation
100 Event (Chen et al., 2020), although debate exists for Archean antiquity of *arrA* (Kulp et al.,
101 2008; Schoepp-Cothenet et al., 2009). Arsenic has therefore become an element of prime interest
102 for geobiology studies as it may hint at early Earth microbial cycling.

103 Analogous environments in modern settings where active As cycling has been identified
104 have been used to better assess the potential for As-based ecosystems. Numerous studies of the
105 hypersaline and alkaline environments of the high-altitude Andean lakes (Farías et al., 2013;
106 Fernandez et al., 2016; Sancho-Tomás et al., 2018; Saona et al., 2021), Searles Lake (Oremland
107 et al., 2005) and Mono Lake (Kulp et al., 2008; Switzer et al., 1998) have advanced our
108 understanding of As cycling. Some of these environments contain microbial mats that can be
109 seen as modern equivalents of primordial ecosystems exhibiting As cycling (Visscher et al.,

110 2020). These modern examples could explain As enrichments in fossilized microbial structures
111 observed for the Archean Dresser Formation stromatolites (Baumgartner et al., 2020) and the
112 Tumbiana stromatolites (Sforna et al., 2014), where the coupling of As cycling with anoxygenic
113 photosynthesis has been hypothesized to be a potential phototrophic pathway before the
114 emergence of oxygenic photosynthesis (Oremland et al., 2009).

115 In the Dead Sea water, potentially toxic trace element concentrations are relatively high
116 (Nissenbaum, 1977) but their levels are not thought to be “seriously limiting to life” (Oren,
117 1983). Adaptations to these elevated concentrations have nonetheless been identified in DNA
118 extracted from subsurface evaporitic units (Thomas et al., 2014). In contrast, As is neither
119 enriched in the brines nor the mud of the modern Dead Sea. Kotova et al. (2016) measured As
120 concentrations of 0.01 mg.L⁻¹ in the Dead Sea Brine, and up to 3 mg.L⁻¹ in shallow Dead Sea
121 mud of the western shore. Similar ranges of concentrations were measured from the eastern
122 shore mud (Abdel-Fattah & Pingitore, 2009).

123 Metalloid-like use by microbes from the Dead Sea was identified in a selenate-breathing
124 anaerobic bacterium isolated from shallow sediments (Switzer et al., 2001). High metabolic
125 diversity was found in microbial mats near and within underwater freshwater springs (Ionescu et
126 al., 2012), including phototrophic communities (green and purple sulfur bacteria, cyanobacteria)
127 and potential metal reducers (mainly associated with Fe-cycling). While life in the Dead Sea
128 brines is strongly limited by hypersalinity and high divalent cation concentrations (Oren, 1999,
129 2010), dilution of the brine by freshwater springs onshore (Adar et al., 2014; Hirshberg & Ben-
130 Ami, 2019) or offshore (Häusler, Noriega-Ortega, et al., 2014; Ionescu et al., 2012), or by heavy
131 rainfalls (Levy et al., 2022; Oren, 1993; Oren et al., 1995), allows diversification of microbial
132 communities and metabolic potential, including the possible use of other metalloids.

133 The Dead Sea lake level has been dropping by ca. 1 m per year for the last 30 years (Abu
134 Ghazleh et al., 2009; Lensky et al., 2005). Freshwater aquifers follow the retreat of the denser
135 Dead Sea Brine as lake level drops and infiltrate the Quaternary lacustrine deposits of the Dead
136 Sea paleolake (Shalev et al., 2006; Yechieli et al., 2006). Inside these evaporitic formations,
137 halite is easily dissolved by the circulating subsurface freshwater, which leads to land instability,
138 epitomized by frameworks of fractures and sinkhole formation along the coasts of the Dead Sea
139 (Closson & Abou Karaki, 2009; Nof et al., 2019). Some circulating freshwater may emerge and
140 form springs of varying chemistry, heat and salinity, depending on their hydrographic specificity
141 (interactions with groundwater, brine, sediments...). The resulting structures are often networks
142 of ponds and sinkholes providing favorable conditions for the development of diverse life
143 (Hirshberg & Ben-Ami, 2019), including microbial communities and microbial mats (Adar et al.,
144 2014; Ionescu et al., 2012; Thomas et al., 2021).

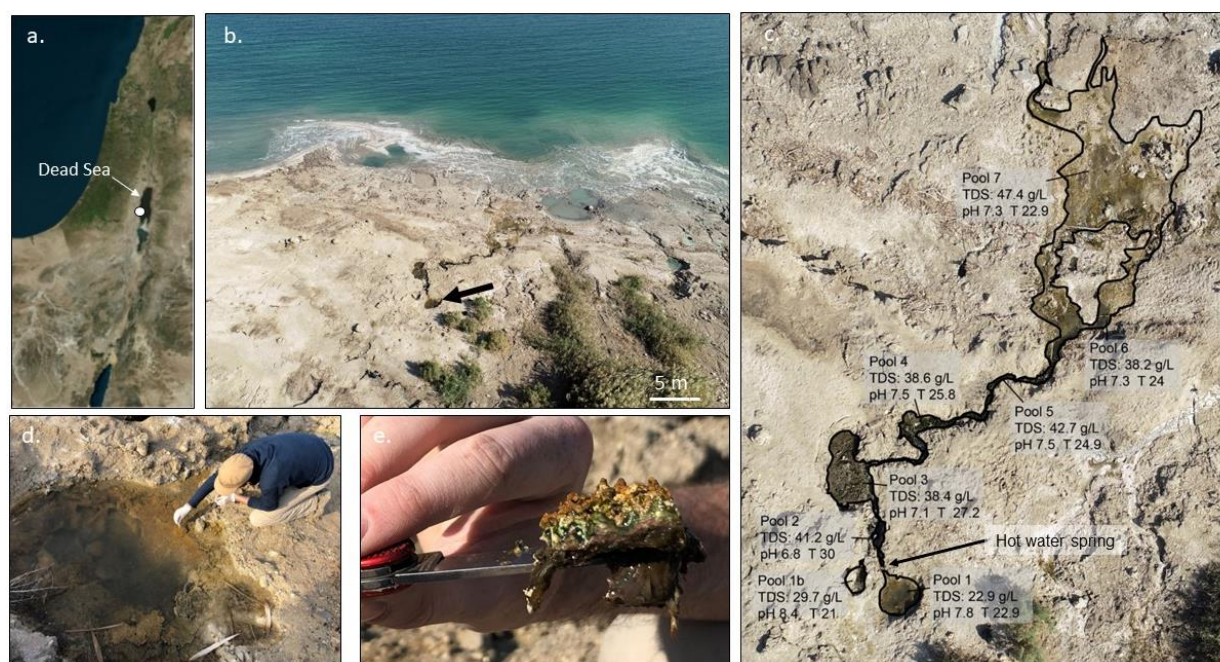
145 We identified As-rich environments and associated microbial mats in the sinkhole
146 systems of Dead Sea western shores. Here, we investigate this actively accreting microbialite
147 environment to determine whether it has the potential to serve as a model system for As
148 biosignature incorporation in living microbial mats, providing needed insight into fossilized
149 counterparts. In this study, we use a combination of imaging techniques (including
150 fluorescent/hyperspectral microscopy), (meta)genomics, mass spectrometry, and synchrotron-
151 based techniques to map the elemental distribution and microbial structure of the As-rich
152 microbial mat. Together, these analyses allow us to assess the characteristics of As and its
153 relationship to intact in situ biological features. Our objective is to better understand the
154 processes leading to the incorporation of As and trace metal (bio)signatures into microbial mats

155 potentially recognizable as analogues of Precambrian ecosystems and ancient microbial
156 stratiform deposits.

157 2 Materials and Methods

158 2.1 Sampling site

159 The investigated sinkhole is located at 59°78'55 and 23°79'00, close to the Ein Gedi Kibbutz
160 (Fig. 1a). It lies within a small system of recently formed sinkholes (named “pools” in Fig. 1b-c)
161 exhibiting biofilms and microbial mats of different colors and textures. At the time of sampling
162 (January 2020), the sinkhole of interest (pool 1 in Fig. 1c) was a 2 m in diameter and 40 cm deep
163 depression at its maximum, situated at an altitude of -431.6 m above sea level (Fig. 1c-d). It was
164 the highest pool of the whole system, it was among the coldest ones (Pool 1, 22.9 °C) and had
165 the lowest salinity (27.9 g.L⁻¹ TDS). No water source or outflow could be located in pool 1.
166 However, the water temperature rose right at the base of the Dead Sea-facing exterior rim of pool 1,
167 where we located an outflow of water (active hot spring) with temperatures reaching 30°C
168 (marked by an arrow in Fig. 1c). This water fed a stream flowing into a series of interconnected
169 ponds downstream (from pool 2 to pool 7), almost all the way to the Dead Sea (temperature and
170 pH measured for the Dead Sea : T = 24.5 °C, pH = 6,5). The bottom of pool 1 was draped by a
171 partly mineralized microbial mat of ca. 2 to 4 cm thickness, immersed in water with an Eh of
172 26.6 mV and a pH of 7.8. The surface of the mat was pustular with brownish to orange mineral
173 clusters (CaCO₃), intertwined at its base by green wavy gel-like laminae on top of a pink wavy
174 lamina. A dark brown to dark grey biofilm layer formed the base of the mat (Fig. 1e).



175
176 **Figure 1.** Photographs of sampling system and location. Location of the sinkhole system (white
177 dot) on the western shore of the Dead Sea, within the Levantine region (a). A network of several
178 ponds formed by evaporite dissolution by circulating fresher water flowing towards the Dead Sea
179 was sampled. Samples and data presented originate from the pool identified by the black arrow
180 (b), named pool 1 in the drone photo showing the sinkhole system and their overall properties

181 (c). Zoomed-in photo of pool 1 (d), and field photo of the well-laminated microbial mat (e).
182 Water circulates from pool 2 to pool 7. However, no water was clearly observed flowing out of
183 pool 1 and pool 1b suggesting a disconnection of these two pools, with a spring slightly above
184 pool 2 feeding pools 2 to pool 7.

185 2.2 Field sampling and sample preparation

186 Microbial mats, water samples, and *in situ* measurements of environmental parameters were
187 collected in January 2020. Fresh sections of the microbial mat were collected in plastic boxes
188 and kept immersed in the pool water. The microbial mat section used for pigment and elemental
189 imaging was subsampled on site and kept cool (4°C) in a plastic vial until resin embedding in the
190 geomicrobiology laboratory of the Earth Science Department at the University of Geneva, a few
191 days after sampling. There, the 1.5 cm long sample was immersed in successive baths of absolute
192 ethanol (99 % purity), and then in freshly opened acrylic LR white resin (Sigma Aldrich®,
193 Merck KGaA, Darmstadt, Germany). The sample was brought to 40 °C for 1 hour and further
194 incubated at 60 °C for 3 days to achieve maximum desiccation. The resulting LR white resin-
195 embedded microbial mat was then engulfed in classic epoxy resin Epo-Tek® 301 (Epoxy
196 Technology, inc., Billerica, MA, USA) and mirror polished.

197 2.3 Epifluorescence microscopy

198 The resin-embedded sample was used to observe natural autofluorescence using a LSM780
199 Airyscan Zeiss microscope and filters adapted to DAPI (excitation wavelength 353 nm, emission
200 wavelength 465 and detection between 400 and 509 nm), APC (excitation wavelength 651 nm,
201 emission wavelength 660 nm and detection between 635 and 700 nm) and Rhodamine
202 (excitation wavelength 558 nm, emission wavelength 575 nm and detection between 562 and 700
203 nm), and processed using the Zen 3.2 imaging software by Carl Zeiss Microscopy GmbH®
204 (Oberkochen, Germany), at the Bioimaging Center of the University of Geneva.

205 2.4 Elemental chemistry of the pool water and bulk microbial mat

206 Water parameters (pH, eH, and temperature) were measured on site during sample collection
207 using a CTD probe. Water samples were filtered with a 0.22 µm pore size filter (Millipore,
208 Merck KGaA, Darmstadt, Germany) and stored in sterile metal free plastic tubes in the dark at 4
209 °C until further analysis. Major anions and cations in the water were measured on a Dionex ICS-
210 3000 (Thermo Scientific, Waltham, MA, USA) ion chromatograph at the University of Geneva.

211 Further elemental analysis was conducted in the Biogeochemistry Laboratory at the Rosenstiel
212 School of Marine, Atmospheric, and Earth Science. All sample and standard preparation were
213 conducted in Class 100 trace metal workstation in a metal-free ISO Level 7 Clean Room using
214 distilled nitric acid (Savillex Acid Purification System, DST-1000) and 18MΩ MilliQ water. The
215 concentration of As in the water sample was determined using a standard addition method
216 following the procedure recommended by Yang et al. (2018). In brief, a 50 µg.L⁻¹ As spike
217 solution was created by diluting NIST-traceable SPEX CertiPrep Solution 2A with 0.16 M
218 ultratrace HNO₃. A seawater certified reference material (CASS-6, NRC Canada) was diluted
219 gravimetrically by a factor of 10× with 0.16M ultratrace HNO₃, resulting in a diluted seawater
220 solution with 0.1 µg.L⁻¹ As. Next, the spike solution was added in variable proportions to six
221 aliquots of this seawater to create a range from 0.1-1.8 µg.L⁻¹ As. Analysis of this suite of spiked
222 CRM solutions was performed using a triple quadrupole inductively coupled plasma mass

223 spectrometry (Agilent 8900 ICP-QQQ) using a UHMI setting of 25. The instrument setup
224 included an integrated autosampler (SPS-4) with HEPA filtration and coverkit, Ni skimmer and
225 sampler cones, and a standard electron multiplier detector. During the analysis, the instrument
226 was operated using Mass Hunter 4.5 Workstation Software (C.01.05). Each measurement was
227 performed in triplicate, with 100 sweeps each, and all reported values had less than 5% Relative
228 Standard Deviation (RSD). Prior to each analysis, instrument tuning was conducted using a
229 tuning solution containing $1 \mu\text{g}\cdot\text{g}^{-1}$ Li, Y, and Tl from Agilent Technologies Tuning solution to
230 optimize signal sensitivity and peak resolution at low, mid, and high m/z ranges. To monitor
231 interference, plasma-derived oxides and doubly charged ions were checked before each
232 analytical batch and kept below 2% and 3%, respectively. Scandium was introduced using
233 Agilent's in-line internal standards kit as an internal standard to monitor instrument drift
234 throughout the analysis. The measurement of As was performed using the mass shifted O_2 gas
235 mode ($^{75}\text{As} \rightarrow ^{91}\text{As}$). Sample counts were corrected for contributions from the blank solution by
236 analyzing an acid blank prepared from the same 0.16M HNO_3 used to prepare the CASS-6
237 seawater dilutions. Counts measured for each of the seven CASS-6 solutions were then regressed
238 against the expected concentrations in the spike of each standard solution. The resulting curve
239 was characterized by a linear relationship ($R^2 = 0.9968$), and the intersection of this curve with
240 the x-axis provided the concentration of As in the unspiked standard reference material (CASS-
241 6) with 96% recovery. Using this CASS-6 verified external 7-point calibration curve, we
242 calculated the concentration of As in the Dead Sea water sample based on measured counts. The
243 detection limit, calculated by the Mass Hunter Software for this analysis was $0.06 \mu\text{g}\cdot\text{L}^{-1}$.

244
245 To analyze the bulk microbial mat composition, approximately 100 mg of dried and powdered
246 samples were weighed into pre-cleaned 30 mL perfluoroalkoxy alkane (PFA) digestion vessels
247 (Savillex, USA). As previously, a two-step, sequential digestion protocol was conducted using
248 ultra-trace grade 30% H_2O_2 and 16 M distilled HNO_3 as described previously (Abdool-Ghany et
249 al., 2023). First, approximately 3 mL of ultratrace H_2O_2 were added to the PFA vessel, the lid was
250 tightly capped, and put on a hot plate set to 115°C for 24 h. After cooling, the PFA vessels were
251 weighed again to assess mass loss during digestion, which was less than 1.7% on average. Samples
252 were uncapped and put on a hotplate set to 70°C in a metal free Class-100 workstation to evaporate
253 H_2O_2 . Next, 3 mL of 16 M distilled HNO_3 were added to each vessel. After tightly capping, sample
254 weights were recorded again, and the vessels were placed on a hotplate set to 135°C for 48 h.
255 After cooling, sample weights were recorded, and the samples were again placed to evaporate on
256 a hotplate set to 70°C . Residual sample was resuspended in 5 mL of ultra-trace 0.16M HNO_3 , and
257 aliquots were diluted volumetrically for analysis of elemental concentrations. Procedural blanks,
258 NIST-Traceable SPEX CertiPrep solutions, and certified reference materials (FEBS-1, NCS-DC-
259 73340, IAEA 413, IAEA 392, DOLT-5) digested in the same manner as the samples were analyzed
260 with every batch of samples to confirm accuracy. Average CRM recovery and detection limit for
261 each element are indicated in Table S1. Based on replicate analyses of certified reference materials,
262 measurement accuracy was within $\pm 4.5\%$ of certified reference values on average. Analyses were
263 made on a triple quadrupole inductively coupled mass spectrometer (Agilent 8900 ICP-QQQ,
264 Agilent, Santa Clara, CA, USA) using a UHMI setting of 8 in He-gas mode on mass for ^{24}Mg and
265 ^{55}Mn , H_2 gas mode for ^{40}Ca , and in O_2 mass shift mode for ^{32}S , ^{75}As , and ^{56}Fe . Scandium was
266 introduced as an on-line internal standard via the Agilent ISTD kit, and plasma-derived oxides and
267 doubly charged ions were maintained below 2 and 3% respectively as described above.

268 2.5 Particle-induced X-ray Emission (PIXE) imaging

269 Experiments were performed on the resin-embedded sample at the AIFIRA Facility (LP2i-
270 Bordeaux, France) with a 3 MeV protons microbeam (Beam diameter = 1 μm , Beam current ~
271 100 pA). The fast raster of the beam allowed elemental mapping of few mm square areas. μPIXE
272 were done with Si(Li) detectors (Raypsec Ltd, High Wycombe, UK) equipped with a Carbon
273 Funny Filter (thickness 500 μm , hole size 2 mm) which detect X-rays emitted from the
274 interaction of protons with the samples. The beam current was set to keep deadtime below 10%
275 on the PIXE detector. μRBS (Rutherford Backscattering spectroscopy) were done with a Silicon
276 PIPS detector (Mirion Technologies, Inc., Atlanta, GA, USA) which detects backscattered
277 protons; it is used for quantification. Data treatment and quantification were done with SIMNRA
278 7.02 (www.simnra.com) and GUPIXWin 2.2.1 (<http://pixe.physics.uoguelph.ca/gupix/main>;
279 Campbell et al., 2010). Maps and image analyses were obtained using combined imageJ and R
280 protocols. The relative grey scale intensity was transformed into a matrix of values for each pixel
281 using the “image to result” command in ImageJ (V. 1.53e), and then processed as surface plots.
282 Pixel matrices were processed and analyzed for each element with R using the raster and
283 rasterVis packages.

284 2.6 Synchrotron-based X-ray fluorescence and XANES spectra analyses

285 The resin embedded sample was brought to the Swiss Light Source, at the Paul Scherrer
286 Institute, Villigen, Switzerland. Synchrotron-based scanning XRF and absorption contrast was
287 performed at the microXAS beamline, using an X-ray energy of 12 keV, focused to $1 \times 1 \mu\text{m}^2$
288 using a Kirkpatrick–Baez mirror system. The scans were recorded in fly scan mode, recording
289 the full XRF spectra every 100 ms with variable step size. The XRF spectra were recorded with
290 single-element silicon drift detectors (Ketek GmbH, Germany) coupled to FalconX pulse
291 processors (XIA LLC, USA). XRF data was fitted using PyMCA (Solé et al., 2007). X-ray
292 absorption near edge structure (XANES) were collected around the following As K-edge regions
293 and step sizes : 11.839-11.86 keV at 0.001 keV steps, 11.86-11.88 at 0.0004 keV steps, 11.88-
294 11.90 at 0.001 keV steps, 11.9-11.95 at 0.002 keV steps and 11.95-12.1 at 0.003 keV steps. Data
295 processing was done with the software Athena, using the corresponding normalization and
296 background removal parameters : $E_0 = 11867.5 \text{ eV}$, 3rd normalization order, pre-edge range -
297 28.522 to -17.110, flatten normalized data and normalization range between 58.490 and 229.190,
298 with 464237.57 edge steps. Rbkg was at 1.0 and K-weight at 2. Spline range were set between 0
299 to 7.767 in k, and s0 to 230.01978 in E. Redox maps were constructed after obtaining XRF maps
300 for arsenic at the following energies: 11850 eV, 11868 eV, 11873 eV, 11880 eV and 11890 eV.
301 Noise on these images was removed on imageJ using the “despeckle” prompt and then divided
302 by the “image calculator” prompt,

303 The relative grey scale intensity of XRF map images was transformed into a matrix of values for
304 each pixel using the “image to result” command in ImageJ (V. 1.53e). Pixel matrices were then
305 processed and analyzed for each element with R using the raster and rasterVis packages.

306 Arsenopyrite (solid mineral), As_2S_2 powder (Arsenic(II) sulfide, Sigma-Aldrich, Merck KGaA,
307 Darmstadt, Germany), As_2O_3 powder (As(III) oxide , Thermo Scientific Chemicals, Waltham,
308 MA, USA), As_2O_5 powder (As(V) oxide, metal base, Thermo Scientific Chemicals, Waltham,
309 MA, USA), and triphenylarsine powder ($\text{As(III)(C}_6\text{H}_5)_3$ (Thermo Scientific Chemicals,
310 Waltham, MA, USA) were used to obtain reference XANES spectra. Powders were mixed with
311 boron nitride and mounted on in nearly 2 mm-thick plexiglass frames.

312 2.7 Hyperspectral imaging of bacterial pigments

313 The resin-embedded sample were scanned by hyperspectral Specim PFD-CL-65-V10E linescan
314 camera (Specim, Oulu, Finland) following the method of Butz et al. (2015). The scanning
315 resolution i.e. the pixel size was 60 μm . We examined the sample and the resin for their spectral
316 absorption to identify pigments. The Relative Absorption Band Depth (RABD) in certain
317 wavelength ranges was calculated from the spectra to quantify relative changes in pigments
318 throughout the sample. RABD620 represents phycocyanin, a pigment produced by cyanobacteria
319 (Sorrel et al., 2021). RABD660-670 is interpreted as total chlorophylls-a, which represents
320 total algal abundance (Butz et al., 2017; Rein & Sirocko, 2002; Zander et al., 2022). The spectral
321 absorption of the surrounding resin was determined and used as background in calculation to
322 remove any potential matrix effect of the resin on the sample spectra.

323 2.8 16S rRNA gene and metagenomic analysis of arsenic-related genes

324 Samples were extracted using the DNeasy PowerBiofilm® Kit (Qiagen, Germantown, MD,
325 USA) following the instructions provided by the company. The extracts were then quantified
326 using Invitrogen Qubit ds DNA HS assay kit (Life Technologies, #Q32851, Grand Island, NY,
327 USA), and sent for amplification of the 16S rRNA gene to Fasteris (Genesupport SA, Geneva,
328 Switzerland) using the primers 515F (5'-GTGYCAGCMGCCGCGGTA-3') and 909R (5'-
329 CCCCgycaattcmtttragt-3') (Yong Wang & Qian, 2009). Samples were then purified,
330 quantified, pooled for library preparation (no PCR cycle to finish the library) and sequenced by
331 Illumina Miseq (1 paired-reads run 2 x 300 bp; Illumina Inc San Diego, CA, USA). Yield and
332 quality controls were within specifications. Samples were then filtered and trimmed using
333 cutadapt (Martin, 2011), assembled and checked for chimeras using dada2 (Callahan et al., 2016)
334 and further analyzed using phyloseq (McMurdie & Holmes, 2013) and vegan (Oksanen et al.,
335 2007) packages with R (R Core Team, 2013), as described in the Open Research Statement
336 below.

337 Metagenomes were obtained from the same extracts using Illumina NovaSeq S4 (2x150;
338 Illumina Inc San Diego, CA, USA) after shotgun Library Prep at the Rush University Genomics
339 and Microbiome Core Facility. Genomic DNA samples were prepared for sequencing by an
340 initial quantification using Qubit 4 Fluorometer (Life Technologies, #Q32851, Grand Island,
341 NY, USA). Library preparation was performed using the Illumina DNA Prep Workflow with
342 UDI indexing (#20018705, 20027213 Illumina Inc San Diego, CA, USA) according to the
343 manufacturer's instructions with 50 ng template input and 5 cycles of PCR. An equal-volume
344 pool of all libraries was then made. The pool was quantified using a Qubit DNA High Sensitivity
345 kit (Life Technologies, #Q32851, Grand Island, NY, USA), and size distribution was assessed
346 using an Agilent 4200 TapeStation System (Agilent Technologies, G2991AA, Santa Clara, CA,
347 USA) using TapeStation D5000 ScreenTape, ladder and assay (Agilent Technologies, # 5067-
348 5588, 5067-5590 and 5067-5589, Santa Clara, CA, USA). The pooled libraries were run on
349 Illumina MiniSeq instrument using MiniSeq Reagent MO Kit, (300 cycles) (Illumina Inc San
350 Diego, CA, USA) run for quality control and libraries balancing purposes. A new pool was made
351 based on the MiniSeq run results, quantified same as described above and sequenced on an
352 Illumina NovaSeq 6000 instrument (300 cycles) (Illumina Inc San Diego, CA, USA), with a 1%
353 phiX spike-in. Raw sequence reads were quality trimmed and filtered using Trimmomatic
354 (v0.39) (Bolger et al., 2014) and assembled de novo using SPAdes (v 3.13) (Bankevich et al.,
355 2012) using the `-meta` option for metagenomic assembly. Reads from each sample were mapped

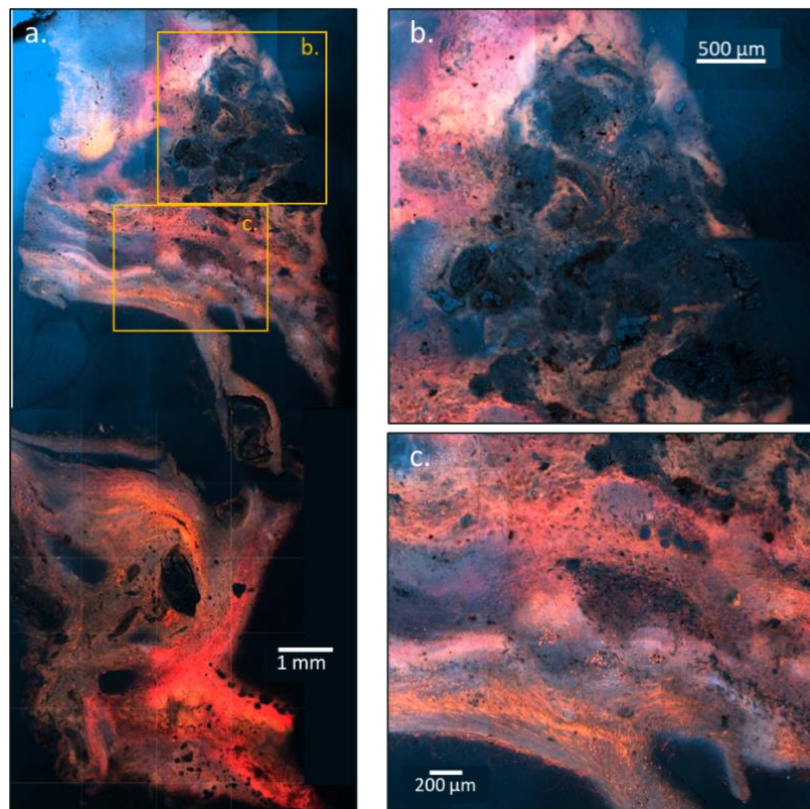
356 to the assembled contigs of each file using BBmap (sourceforge.net/projects/bbmap/) and
357 converted to sorted BAM files using SAMTools (Danecek et al., 2021). The depth profiles for
358 each assembly were generated using the jgi_summarize_bam_contig_depths tool provided with
359 Metabat2 (Kang et al., 2015). Binning was done using Metabat2 (v 2.15) (Kang et al., 2015)
360 using default setting. Completeness and contamination of genomes was estimated with CheckM
361 tool (v2) (Parks et al., 2015). Taxonomic classification of metagenomic bins was performed with
362 GTDB-Tk (v 2.1.1) (Chaumeil et al., 2020). Annotation of bins was done with Prokka V
363 (Seemann, 2014), BlastKoala (Kanehisa et al., 2016) and EggNOG-mapper v; (Cantalapiedra et
364 al., 2021). To obtain annotation of proteins found in unbinned contigs, open reading frames were
365 called using Glimmer (Delcher et al., 2007) from the assembly result and subsequently annotated
366 using GhostKoala (Kanehisa et al., 2016) and EggNOG-mapper (Cantalapiedra et al., 2021).

367 **3 Results**

368 3.1 Microbial mat composition

369
370 The microbial mat consisted mostly of organic matter (Fig. 1e). It included pigment-rich EPS,
371 with occasional localized mineral clusters (upper right corner, Fig. 2a-b), and more isolated
372 detrital minerals and concretions (Fig. 2c). The sample was partially mineralized on its surface,
373 as could be seen by the orange to brownish pustular structures in the hand samples (Fig. 1d).
374 These minerals had a blue autofluorescence when viewed using a DAPI filter (excitation 350-
375 400 nm; emission 420-480 nm), which is typical of calcium carbonates (Fig. 2a-b) further
376 identified as aragonite by Raman Spectroscopy (not presented here). These mineralized areas
377 occurred in the upper right corner of the sample section (Fig. 2a) in rather heterogeneous
378 lithofacies composed of aragonite needles partially to completely agglomerated as concretions
379 reaching ~100 μm in length (Fig. 2b, Fig. S1). In this mineralized region of the sample (Fig. 2b),
380 organic matter is more dispersed as supported by low yellow to red autofluorescence (filters for
381 Rhodamine and APC) compared to the rest of the investigated sample.

382 High-resolution epifluorescence imaging (Fig. S1) revealed a common occurrence of
383 dinoflagellates and diatom shells in the top 5 mm of the sample. The sample also presented
384 cavities and voids (dark blue to black in Fig. 2), observed particularly the middle of the sample,
385 possibly triggered by the resin hybridization protocol. Filaments of various lengths and diameters
386 were present all along the sample, displaying red and yellow autofluorescence (using APC and
387 Rhodamine filters). These filaments were either structureless, organized around voids, or
388 observed in well-ordered, parallel laminae. The resulting filamentous network formed well-
389 identifiable wavy textures (see Fig. 2c, and in the bottom part of the sample, Fig. 1e and Fig. 2a).
390 Coccoids, interpreted here as *Cyanobacteria* based on autofluorescence, occasionally formed
391 denser aggregates. Photopigments were identifiable all the way down the core, with higher
392 autofluorescence observed at the bottom. This downward trend of autofluorescence intensity was
393 confirmed by hyperspectral images (Fig. S2) of chlorophyll a, and b, and phycocyanin. Overall,
394 yellow-red autofluorescence visualized the EPS content and the structure of the mat, while blue
395 (Fig. 2b-c) represented carbonate minerals. In the bottom part of the sample, these blue zones
396 were less present and large black patches/islands showed detrital minerals (silicates).

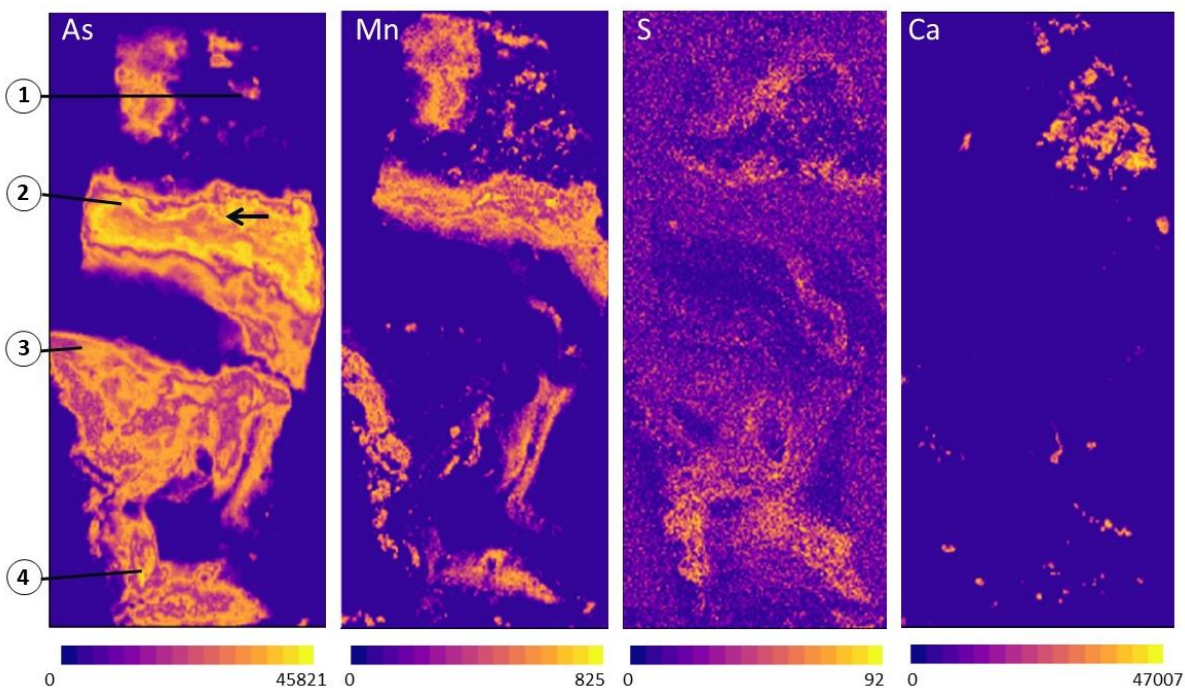


397

398 **Figure 2.** Epifluorescence microscopy images of the microbial mat from the surface of the
399 microbial mat (top of image (a)) to bottom of the mat (bottom of the section in (a)). The
400 unstained mat was imaged using a combination of the following filters (filter for DAPI: blue
401 color showing autofluorescence of calcium carbonate minerals; filter for APC: red color covering
402 autofluorescence of chlorophyll, allophycocyanin and phycocyanin; filter for Rhodamine: yellow
403 color covering autofluorescence of cyanobacterial phycoerythrin and phycoerythrocyanin). The
404 stacked images highlight most photosynthetic pigments in yellow-red, while minerals (mainly
405 aragonite) are colored in blue. (b) Zoom on the frame labelled (b.) in photo a. (c) Zoom in the
406 frame labelled (c.) in photo a.

407 3.2 Elemental distribution and local chemical enrichment

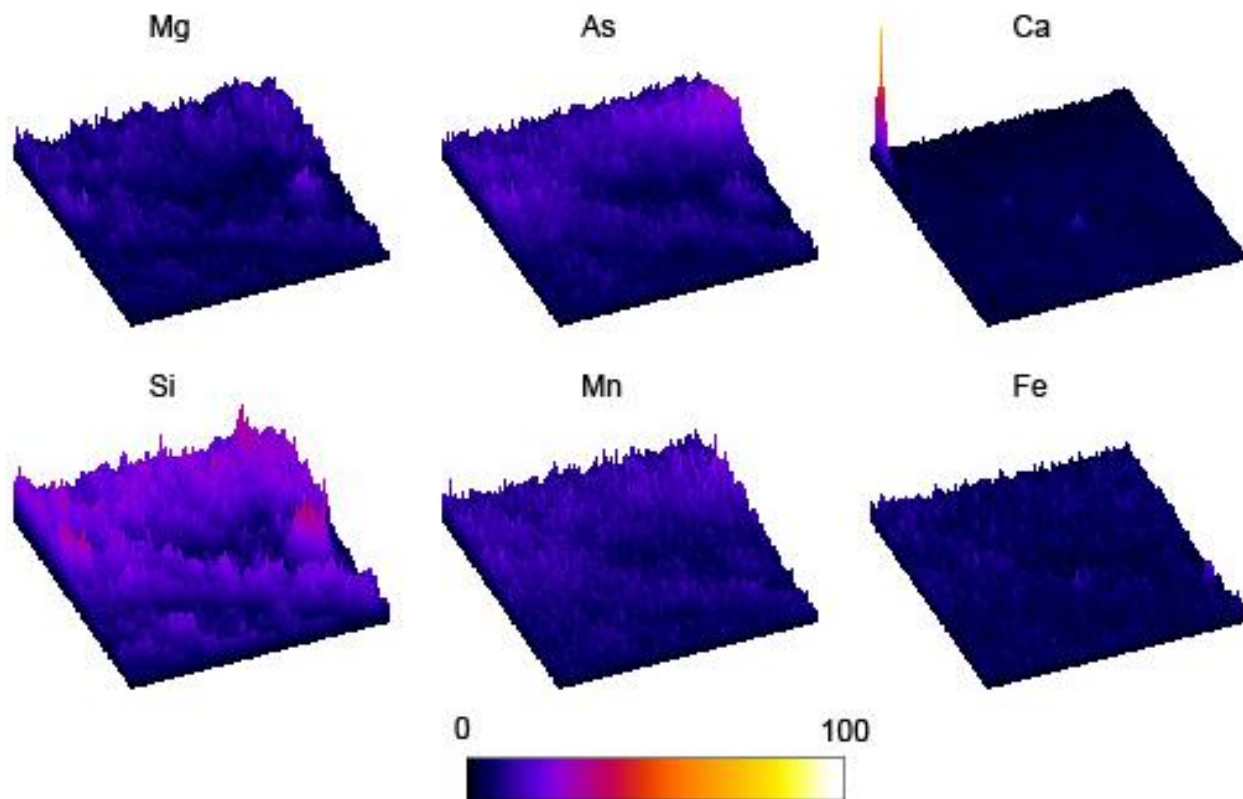
408 Synchrotron-based XRF indicates that As is enriched in most of the EPS, but to varying degrees
409 across the sample (Fig. 3). The As content reaches a maximum of 15700 ppm in the middle
410 lamina (arrow Fig. 3 and Fig. 4), much higher than other trace elements (e.g., Mn: 2200 ppm, Fe:
411 660 ppm; Table 1). The As concentration was more than 390× than the bulk concentration
412 measured for the whole sample (40.1 ppm; Table 1), and more than 6.5 million× the
413 concentration measured in the water from pool 1 at the time of sampling ($2.39 \mu\text{g}\cdot\text{L}^{-1}$; Table 1).
414 Manganese was often co-enriched with As in many occurrences in the mat, particularly in the
415 max-As layer (Fig. 3), where it reached a factor of 5× compared to the bulk sample composition
416 (389.3 ppm Mn). Sulfur enrichment in the As-rich layer was relatively minor (2.5× compared to
417 the bulk at 7126.5 ppm S) and reached a maximum in the bottom part of the mat. Calcium was
418 only mapped within mineral phases in Fig. 3, but Ca-enrichment was also observed in the EPS
419 (Fig. 4), although it does not correlate with the As-Mn-rich phase.



420

421 **Figure 3.** Synchrotron-based XRF maps of the microbial mat showing strong As enrichment,
422 associated to a certain extent with Mn concentrations. CaCO minerals are mainly located in the
423 top right corner and associated with Ni and K (not shown). Sulfur increases in the bottom of the
424 mat but has overall relatively low concentrations. The color scale indicates XRF intensities from
425 the detection limit (purple) to the maximum measured (yellow). Black arrow in As frame shows
426 the location of the PIXE analyses presented in Figure 5, and numbers correspond to XANES
427 analysis points (Fig. 6).

428



429

430 **Figure 4.** Surface plot of elemental concentrations measured by PIXE mapping in the As-rich
 431 zone (arrow in Fig. 3). It shows co-enrichment in Si, As, Mn and Mg. Fe and Ca were also
 432 detected. The PIXE spectra also show peaks of Na, S, Cl, Br, Rb, Sr, and very faint Cu and Zn
 433 (see supplementary material Fig. S4). Images are 250 μm x 250 μm . The color scale shows
 434 relative intensity from below detection limit (black) to maximum (white) values.

435

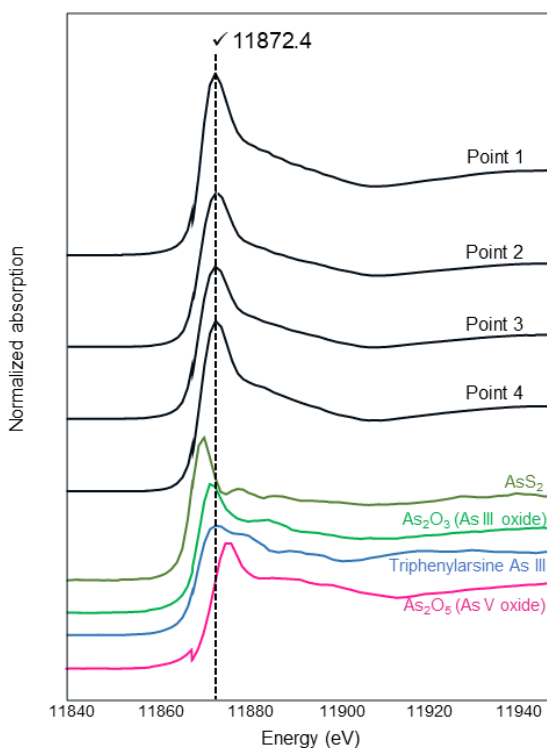
	water ($\text{mg}\cdot\text{L}^{-1}$)	bulk mat ppm ($\text{mg}\cdot\text{kg}^{-1}$)	As-rich zone (PIXE)		EPS to bulk enrichment	EPS to water enrichment
			ppm ($\text{mg}\cdot\text{kg}^{-1}$)	limit of detection (ppm)		
Mg	3.54×10^3	31.8×10^3	152×10^3	506	4.80	43.0
Ca	2.20×10^3	166×10^3	25.5×10^3	61.3	0.15	11.6
S	514	7.12×10^3	17.9×10^3	201	2.52	34.9
Mn	-	399	2.25×10^3	123	5.77	-
Fe	-	3.19×10^3	660	15.5	0.21	-
As	2.4×10^{-3}	40.1	15.7×10^3	80.8	392	6.54×10^6

436 **Table 1.** Chemical composition of the mat water and bulk mat (as measured from ion
 437 chromatography and QQQ-ICP-MS) and specific As-enriched zone (as measured by PIXE).

438 Concentrations of sulfur in the bulk mat samples are informational, all other elements were
439 measured using replicate analyses of reference materials (Table S1).

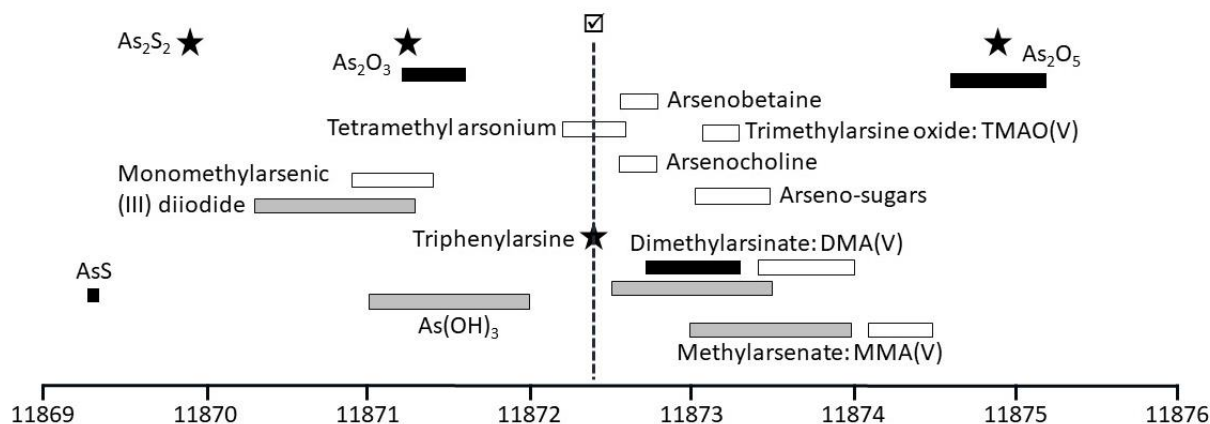
440 Over twenty XANES spectra were acquired across the sample. They showed similar patterns
441 with a white line peak energy consistently measured at 11872.4 eV and a single peak shape as
442 shown for the four points spread from the top to the bottom part of the mat (Fig. 3 and Fig. 5).
443 The curve shape of all measured points is relatively similar to that obtained for As_2O_5 , but with a
444 difference in the As white line peak energy (measured at 1874.9 eV). The obtained white line
445 peak energies for the standards are 11871.2 eV for As_2O_3 , 11869.9 eV for AsS_2 and 11872.4 eV
446 for triphenylarsine. The peak energy of the triphenylarsine is thus identical to the peak energy of
447 the points measured throughout the sample, although the shape of the curve is radically different.
448 These data are presented in Fig. 6 and compared to other published white line peak energies for
449 common reference material, including organoarsenic compounds that were not measured during
450 this study. Based on these comparisons, the white line measured in this study better matches that
451 of As(V) organoarsenic species. Values obtained from methylated arsenate (in particular
452 tetramethylarsonium) overlap or are very close to those measured across the mat. Other
453 organoarsenic species, such as arsenobetaine and choline, also show close white line peak energy
454 values but published spectra differ in overall shapes, as discussed in the next sections. Published
455 examples of As(V) organic compounds like methylarsonate, dimethylarsinate and trimethylarsine
456 oxide (MMA(V), DMA(V) and TMAO respectively) show similar shapes, with a high intensity
457 peak followed by a linear behaviour between 11875 and 11900 eV, and maximum energy peaks
458 that may contribute together to the observed wide peak measured in the mat (Jahrman et al.,
459 2022; Smith et al., 2005).

460



461

462 **Figure 5.** XANES spectra of As across the mat (see fig. 3 for localization), and in reference
463 materials. The broken line refers to the identical white line peak energy (11872.4 eV) obtained
464 for all points measured throughout the sample.



465

466 **Figure 6.** White line energies (in eV) of reference As material including material measured in
467 this study (stars), from Smith et al. (2005; white bars), Bacquart et al. (2007; black bars) and
468 Bacquart et al. (2010; grey bars). Measured whiteline across the mat (see Fig. 5) is represented
469 by the broken line and ticked box.

470

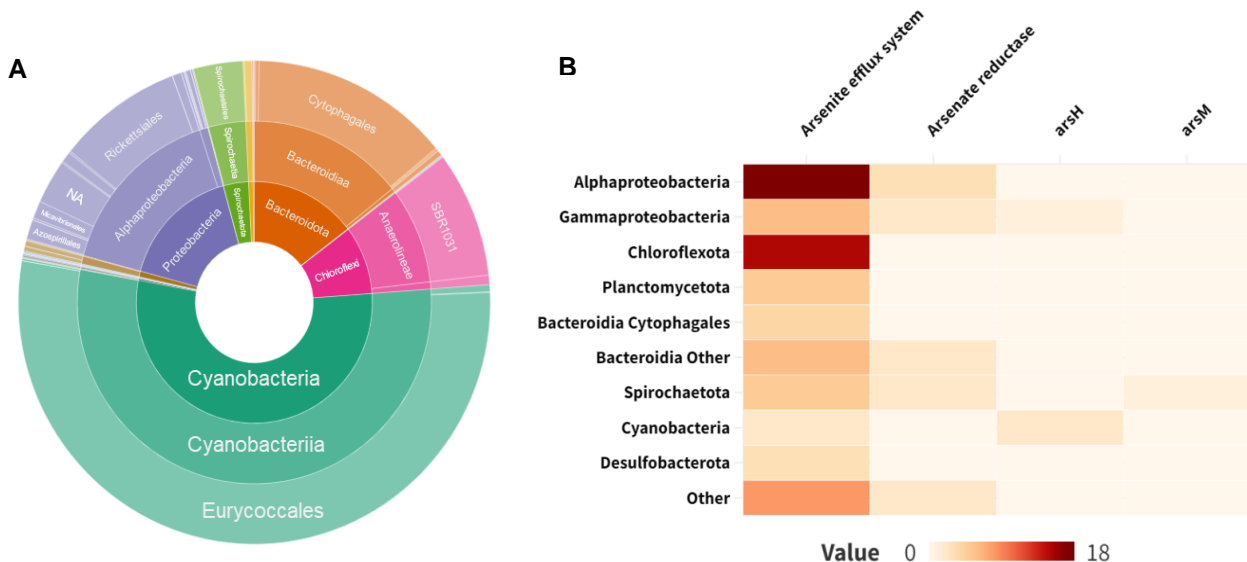
471 3.3 Hyperspectral imaging of bacterial pigments

472 Several spectral absorption troughs in the spectral profiles of the sample as well as of the
473 embedding resin were identified (Supplementary material Fig. S2). The fact that the resin itself
474 has a specific spectral profile means that the resin is absorbing light at certain wavelengths, more
475 specifically at 560-570 nm, 630 nm, 710 nm, 820 nm, 870 nm and 915 nm. The sample absorbs
476 light at wavelength of 550 nm, 620 nm, 660 nm and 915 nm. Based on these data, the presence
477 of phycocyanin, the blue pigment produced by cyanobacteria, is observed in the lower part of the
478 sample (Fig. S3, RABD₆₂₀). Further, the chlorophyll-a and its degradational products (e.g.,
479 pheophytin-a, pheophorbide-a, pyropheophytin-a and pyropheophorbide-a) were identified in the
480 same region as the cyanobacterial signal (Fig. S3, RABD₆₆₀). The green pigments are
481 representing photosynthetic primary productivity. These two pigments are present in the sample
482 with high confidence as the resin spectral profile showed no absorbance in these wavelengths,
483 thus no interference. The bacteriochlorophyll-c,d and e (RABD₇₁₅) produced by green sulphur
484 bacteria cannot be assessed as we observe an interference with the resin absorption in the same
485 wavelength (Figure S3, RABD₇₁₅ and RABD₈₂₀, Fig. S2). The resin signal is here represented by
486 one of its several absorption troughs – RABD₈₂₀ (Fig. S3, RABD₈₂₀). No absorption was
487 observed at the wavelengths specific for the bacteriopheophytin-a, which would show the
488 presence of purple sulphur bacteria. Thus, no anoxic primary producers are found in the sample,
489 only cyanobacterial and photosynthetic primary production.

490 3.4 Genetic composition of the mat

491 The 16S rRNA gene sequences obtained from this mat show a composition of *Cyanobacteria*
 492 predominantly (57 %), *Alphaproteobacteria* (17 %), *Bacteroidota* (15 %), *Chloroflexi* (10 %)
 493 *Spirochaeta* (4 %) and *Gammaproteobacteria* (0.8 %). The overall abundance of *Cyanobacteria*
 494 matches the observations from the field, smear slides and fluorescence microscopy (Fig. 1e and
 495 2). A few phototrophic organisms other than *Cyanobacteria* have potentially been identified
 496 within the *Alphaproteobacteria* class as *Rhodobacterales* (0.7 %) and *Chloroflexales* (0.7 %).
 497 Additionally, a few halophilic purple sulfur bacteria affiliated to *Halochromatium* were
 498 identified (0.1%). No clade or taxa known to cycle As in a dissimilatory way was identified.

499 A total of 2190 metagenomic bins were obtained from the 12 mat samples. The metabolic
 500 potential of these organisms will be discussed in a separate study. Genes related to As processing
 501 were identified in 94 bins in our microbial mat (pool 1). Of these, 70 were affiliated to the
 502 arsenical resistance operon repressor and 20 could be linked to *arsB* arsenite efflux system
 503 (including arsenite efflux pump, arsenite-antimonite *arsAB* efflux family transporter, arsenite
 504 transmembrane transporter activity, arsenite-activated ATPase *arsA* and arsenical-resistance
 505 protein). Additionally, 11 bins contained an arsenate reductase gene, 3 bins associated to the
 506 arsenical resistance protein *arsH* encoding for methylarsenite oxidase, and 1 to As methylase
 507 *arsM*. No bin affiliated with any energy-gaining system from As cycling could be found.
 508 *Alphaproteobacteria* and *Chloroflexia* had a large number of hits for arsenite efflux systems, but
 509 all taxa that could be linked to an As cycle-related bin unsurprisingly had some bins associated
 510 with an arsenite efflux system. Finally, arsenate reductase was found for *Alphaproteobacteria*,
 511 *Gammaproteobacteria*, *Bacteroidia* and *Spirochaeta*. *ArsH* was only tied to
 512 *Gammaproteobacteria Halothiobacillales* and *Cyanobacteria (Synechococcus)*, and the *arsM* hit
 513 was connected to *Spirochaeta (Alkalispirochaeta* genus).



514

515 **Figure 7.** Phylogenetic diversity and As functions of the microbial mat. (a) Genomic affiliation
 516 from the microbial mat using 16S rRNA gene sequences and (b) from As-associated genes

517 obtained from metagenomic sequencing and including genes from the arsenite efflux system,
518 arsenate reductase, *arsH* and *arsM*.

519 **4 Discussion**

520 4.1 Microbial mat structure and composition

521 At the time of collection, the mat was located at the margin of an active hot spring (Fig. 1c). It
522 was in the uppermost pool (pool 1; Fig. 1c) of a system consisting of a series of seven pools
523 seemingly connected by a small stream flowing into the Dead Sea. However, no connection
524 could be observed between pool 1 and the other pools. Based on temperatures, salinity and pH,
525 we interpret that pool 1 is likely to be disconnected from the underlying system (pool 2 to pool
526 7). This fate is experienced by many similar sinkholes in the surrounding area (e.g. pool 1b; Fig.
527 1c) and above, given the rapidly declining Dead Sea level (Al-Halbouni et al., 2021; Nof et al.,
528 2019). This stranding status likely influences the ability to form structured and mineralized mats
529 (which are not observed in the pools below pool 1) and, therefore, the overall chemical, physical
530 and biological characteristics of the sample.

531
532 The mat is not structured in continuous isopachous lamina, rather it shows patchy structures,
533 except for the marked horizontal As-rich lamina. Overall, it consists of EPS highly enriched in
534 Mg and Si (Fig. 4), a feature observed in EPS of the Dead Sea shores (Thomas et al., 2016).
535 Interestingly, Mg-Si enrichments have been commonly described in (mineralizing) microbial
536 mats (e.g. Arp et al., 2003; Kazmierczak & Kempe, 2003; Kempe et al., 2011) where a
537 transitional Mg-Si phase, often referred to as “amorphous Mg-Si phase” precedes the formation
538 of carbonate minerals (Bontognali et al., 2010; Pace et al., 2018; Zeyen et al., 2015). This
539 enrichment has been interpreted as a transitional phase that enhances biofilm mineralization by
540 CaCO₃ precipitation (Pace et al., 2018; Suosaari, Lascu, et al., 2022). In the Dead Sea, heavy Mg
541 enrichment (up to 152,000 ppm) is to be expected given the extreme concentration of Mg²⁺ in the
542 environment (Ionescu et al., 2012) and in the pond water (Table 1). Silicon concentration is not
543 high in the Dead Sea environment compared to other elements (5.1 mg L⁻¹ in average in the
544 water column; Moller et al., 2007), but microbial EPS is commonly enriched in Si, potentially
545 fed by dissolving diatom frustules (present in the mat, Fig. S1). This could explain the high [Si]
546 measured in specific laminae within the mat by PIXE (up to 409,000 ppm, Table 1, Fig. 4).
547 Calcium carbonate precipitation in this context may result in localized rise of alkalinity that may
548 well be triggered by abiotic processes (Belmaker et al., 2019) or microbial activity (e.g. Glunk et
549 al., 2011).

550 Redox sensitive elements (e.g. Mn, Fe, As) are not clearly structured across a depth-gradient
551 along the mat, but rather co-exist at similar levels, pointing to dynamic electron cycling at the
552 mat scale and probably to passive metal binding of by EPS, as described by Sforza et al. (2016).
553 Photosynthetic pigments are distributed throughout the sample. It remains to be resolved whether
554 the presence of photosynthetic pigments in the deepest part of the mat is associated with ongoing
555 oxygen production or is a relic of past activity. Interestingly, the maximum presence of
556 phycocyanin and chlorophyll was measured by hyperspectral imaging in a layer lying below 8
557 mm (Fig. S2). In addition, 16S rRNA gene sequence data show an abundance of anaerobic
558 communities, supporting a complex system structured in dynamic microniches that likely depend
559 on diel cycles, and/or alternate spectral niches (e.g. Wong et al., 2015). Organisms involved in

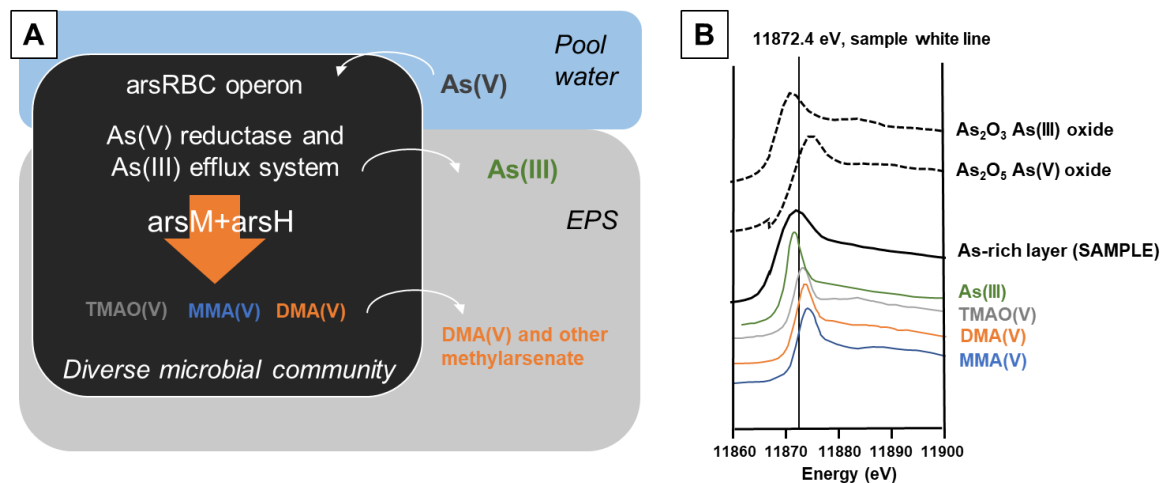
560 oxygenic photosynthesis include phycocyanin and chlorophyll-producing *Cyanobacteria* (Fig.
561 7). Other phototrophic organisms have also been detected, such as carotenoid-bearing
562 heterotrophic *Rhodobacterales* likely involved in the reddish lamina of the mat, filamentous
563 anoxygenic phototrophic of the order *Chloroflexales* (0.7% in the sample, Fig. 7) and few
564 potentially anoxygenic *Halochromatium* members. Hyperspectral imaging allows a more
565 detailed localization of specific pigments (chlorophyll vs phycocyanin, Fig. S3) but does not
566 provide reliable results for bacteriochlorophyll pigments found in anoxygenic phototrophs due to
567 the emission of the acrylic resin employed.

568 4.2 Arsenic cycling: no arsenotrophy but common arsenate detoxification

569 The absence of arsenotrophic organisms in the 16S rRNA dataset does not explain the
570 localization of significant As enrichments, nor does it suggest a link with anoxygenic
571 phototrophic organisms, as recently observed in the purple mat of Laguna La Brava, in the
572 Atacama Desert in Northern Chile (Visscher et al., 2020). Genes that relate to arsenotrophic
573 metabolisms (*arr*, *arx* or *aio*) could not be detected either. Instead, identified As-associated
574 genes point toward common detoxification processes conducted by a variety of organisms.
575 Arsenic resistance in prokaryotes is generally conferred by an arsenate reductase and the *arsRBC*
576 operon, which provides an overall control for the arsenite efflux system (Andres & Bertin, 2016;
577 Mukhopadhyay et al., 2002). Bins associated with this pathway were widely found in our dataset
578 (Fig. 7). Our data also show the presence of the less common *arsA*, that makes the efflux more
579 efficient and confers a higher level of As resistance through the *arsRDABC* operon
580 (Bhattacharjee & Rosen, 2007). In the sample, this gene was only found to be associated with
581 *Cyanobacteria* and one *Euryarchaeota* (Table S1). Additionally, other *ars* genes linked to
582 organoarsenical detoxification were detected in a limited number of bins, and associated to *arsM*
583 and *arsH*, affiliated to *Spirochaeta* of the *Alkalispichoeta* genus for *arsM*,
584 *Gammaproteobacteria Halothiobacillales* and *Cyanobacteria Synechococcus* for *arsH* (Fig. 7).
585 Methylation of arsenic is found in all kingdoms, following Challenger's mechanism (Challenger,
586 1945), which for As involves the reduction of As(V) followed by successive oxidative and
587 reductive methylations steps from As(III), leading to formation of methylated arsenite and
588 arsenite, and ultimately to its final product DMA(V). Some of these intermediate steps were
589 summarized by Wang et al. (2015) in bacteria, and involve genes like *arsM* and *arsH* (Chen et
590 al., 2015; Qin et al., 2006; Yang & Rosen, 2016). *ArsM* is a microbial arsenite S-
591 adenosylmethionine methyltransferase that catalyzes the formation of methylated compounds
592 from As(III), with volatile trimethylarsine as end product (Qin et al., 2006). In this study,
593 intermediate methylated compounds that have been described corresponded to the low-toxicity
594 TMAO and DMA(V), commonly found as trace As substances in organic tissues (e.g. seafood ;
595 Luvonga et al., 2020; Schmidt et al., 2018). The *arsH* gene likely provides resistance to toxic
596 methylated and aromatic As(III) by oxidation of trivalent organoarsenical compounds derived
597 from herbicides and antimicrobial growth promoters (Chen et al., 2015) into low-toxicity
598 pentavalent MMA(V). Therefore, we describe a community potential for As detoxification
599 through arsenate reduction into arsenite and efflux out of the cell, either as arsenite or as As(V)
600 methylated compounds (Fig. 8A). In particular, DMA(V) is commonly described as an efflux
601 product for microalgae in aquatic environments (Filella et al., 2023; Wang et al., 2015). The
602 corresponding As molecules that could be expelled based on our dataset all have XANES peaks
603 that could contribute to the signature obtained for the As-rich layer of the pool 1 sample (Fig.
604 8B). Maximum peak energies for the XANES spectra published by Smith et al., (2005) lie

605 between 11871 eV (for As(III)) and 11874.5 eV (for MMA(V)), with a one-phased to two-
606 phased post-peak linear descent between 11875 and 11900 eV. Comparison of our coupled
607 metagenomic and synchrotron data with published data suggests that such signature could be the
608 result of an efficient detoxification process leading to the efflux and preservation of
609 organoarsenic molecules such as MMA(V), DMA(V) and TMAO in the EPS matrix of the mat.

610



611

612 **Figure 8.** Interpretation of As cycling and species in the Dead Sea mat. (a) Schematic summary
613 of hypothesized As cycling from As(V) rich pool water to immobilization in EPS as
614 organoarsenic. The organoarsenic species DMA(V), TMAO (and MMA(V)) may be formed
615 through identified *arsM* and *arsH* genes identified in the metagenomic pool. (b) XANES spectra
616 of putative organoarsenic molecules along with As(III) (all taken from Smith et al., 2005) with
617 the sample and reference material measured during this study.

618 The As redox state obtained from synchrotron-based redox maps across the mat supports an
619 overall As(V) occurrence throughout the mat (Fig. S5). XANES white lines are in accordance
620 with the presence of As(V) under the form of pentavalent organoarsenics (Fig. 6 ; Bacquart et al.,
621 2007, 2010; Smith et al., 2005). Nevertheless, As(III) cannot be completely ruled out based on
622 XANES signatures, and would be supported by our metagenomic data, which are generally
623 enriched in bins associated to the arsenite efflux system. The stability of this As(III) may
624 however be hindered by the oxic conditions that prevailed in the water of pool 1 at the time of
625 sample collection. Additionally, the overall role of EPS in binding and transforming As is
626 complex. Studies show that EPS production and composition are affected by toxic metalloids
627 like As (Deepika et al., 2016; Naveed et al., 2020). In particular, Deepika et al., (2016) show
628 functional and morphological changes for polysaccharides, proteins and uronic acid of EPS
629 produced by *Rhizobium radiobacter* exposed to As. These compounds all have affinities or
630 functional groups able to bind cations (Naveed et al., 2019; Yan et al., 2017). Naveed et al.
631 (2020) reported EPS production increase and sorption and transformation of As through binding
632 to specific functional groups for cyanobacteria *Synechocystis*. Some of these transformation
633 involved As(III) oxidation and As(V) reduction in As-spiked solution containing extracted EPS.
634 Such interactions complicate our understanding of As redox cycling and detoxification processes
635 in complex and diverse environments such as our microbial mat.

636 All data taken together point to a mechanism of As-enrichment in the mat involving
637 detoxification process through As(V) uptake, reduction to As(III) and methylation in
638 organoarsenic (V) molecules and additional As binding by EPS. The association of manganese
639 with As observed in μ PIXE and μ XRF remains unexplained. It is likely that environmental Mn
640 oxides influence the oxidation of arsenite released from the cells. Poorly crystalline Mn-oxides
641 were shown to oxidize As(III) at varying levels, depending on the Fe(II) content of the medium
642 (Wu et al., 2018). If the waters of pool 1 contain high concentrations of Mn compared to Fe, such
643 chemistry may affect competition between Mn and Fe for As sorption, and favor interaction with
644 Mn. Future analysis of trace metal composition of water would be useful to elucidate these
645 dynamics.

646 4.3 Origin and significance of the arsenic signature

647 The reason for the extreme As enrichment in the mat, together with its spatial restriction to a thin
648 horizontal lamina, remains to be determined. The combined redox (Fig. S5) and metagenomics
649 data (Fig. 7b) argue against an arsenotrophic process, which could be fueled by anoxygenic
650 photosynthesis. Arsenotrophy would have produced a different redox state of As, associated with
651 specific genes, as observed in environments involving active As-based metabolisms (Sancho-
652 Tomás et al., 2018; Visscher et al., 2020). The extreme As concentration measured in the mat of
653 pool 1 is also surprisingly high (15708 ppm) compared to lower values obtained in the current
654 pool water (0.0024 mg.L^{-1}). Low temperatures compared to neighboring pools support a
655 disconnection of the sampled pool/sinkhole from the hydrological system linking downstream
656 pools. These systems form when circulating groundwater makes its way to the surface through a
657 network of porous environments allowed by the dissolution of the evaporitic substrate. The
658 springs emerge sporadically and may cease fairly quickly or persist for a longer period. The size
659 of the system (ponds and streams) is a function of the intensity of flow, the density of water
660 networks and the stability of a system (Ionescu et al., 2012; Yechieli et al., 2006). As water
661 flows continuously in a region, it dissolves more minerals and increases the size of ponds and
662 sinkholes. However, many systems can be abandoned due to the rapid dynamics of water
663 circulation powered by seasonal variations in precipitation/evaporation, associated flash floods,
664 and subsurface subsidence that can be generated in the evaporitic and calcareous undergrounds
665 (e.g. Abelson et al., 2017; Al-Halbouni et al., 2021; Yechieli et al., 2006; Zilberman et al., 2017).

666 We here hypothesize that the pond hosting the studied mat has been recently isolated from the
667 local hydrological system, which explains the variation between local As concentrations and the
668 current As concentration in the pond water and the low temperature. Recent stranding could also
669 explain the specific horizontal layering of As enrichment. A potential scenario is that an As-rich
670 water source flowed into this system for a limited time, leading to the production of an As-
671 enriched microbial mat laminae. Regionally, localized and sporadic As enrichments are not
672 uncommon, particularly in fractured bedrocks along fault zones (e.g. Sidle et al., 2001), a
673 situation analogous to that of the eastern Dead Sea subsurface. For example, As is found
674 enriched to a similar extent in a dry mat collected a few meters south of pool 1, in a dry sinkhole
675 system (50.19 ppm). Arsenic enrichment may also be associated with anthropogenic activity, in
676 particular from pesticides/herbicides. Keeping in mind that the Dead Sea earned its name on the
677 merit of the scarcity of life forms, pesticides and herbicides are never needed in its vicinity.
678 Anthropogenic sources of arsenic are conceivably carried into the Dead Sea by flashfloods from
679 its relatively large drainage, yet this is not represented in lake brine concentrations. It still
680 remain virtually impossible with our current dataset to specify the original source of As, be it of

681 organic or inorganic origin. All we can suggest is that a sporadic increase in As concentrations in
682 a spring would have triggered a protective response to As by microbial mat communities and,
683 therefore, a rapid As-immobilization in the exposed EPS layer. Further mat growth could then
684 carry on. The transient nature of As enrichment in the environment could also be the reason for
685 the lack of evidence of an established arsenotrophic community as observed in stable As-rich
686 environments such the Salar de Atacama, Searles or Mono lakes (Kulp et al., 2008; Oremland et
687 al., 2017; Visscher et al., 2020).

688 4.4 Significance for Precambrian signature

689 The intensity of As concentrations, focused in a millimetric EPS layer of the microbial mat
690 colonizing a Dead Sea pond is remarkable and the development of biotechnological engineering
691 using biofilms for As water decontamination (Ahsan et al., 2012; Singh et al., 2021) presents an
692 interesting area for future research. In some cases, As incorporation may occur through
693 metabolic use, detoxification mechanisms, and arsenotrophy. For instance, in the Salar de
694 Atacama microbialites of Laguna Brava, As (under the form of arsenate and arsenite) was not
695 found to associate with other trace metals, like calcium, silicon, and iron, in organic features,
696 leading the authors to suggest a microbially mediated As cycle, either through detoxification or
697 As-based metabolic pathway (Sancho-Tomás et al., 2018). In the sample from pool 1 in the Dead
698 Sea, synchrotron XRF results showed no co-occurrence of As and other metals except for Mn
699 (Fig. 3), which in concert with XANES and metagenomic data suggest a detoxification process
700 rather than As-based metabolic pathways. Thus, we here show that spatially localized As
701 enrichments can occur in mats where no arsenotrophic activity can be detected, implying that
702 other mechanisms beyond arsenotrophy are consistent with intense As enrichment in
703 microbialites. Here, they involve As detoxification by a suite of diverse microorganisms (Fig. 7).
704 Such a process could have occurred in Paleoproterozoic settings given the fact that As(III)
705 detoxification processes are considered to have appeared early in the history of life (Chen et al.,
706 2020; Zhu et al., 2014). The case of the 2.7 Ga Tumbiana environment, where independent lines
707 of evidence suggest the presence of oxidative conditions (Eigenbrode & Freeman, 2006; Stüeken
708 et al., 2017; Thomazo et al., 2011) could also be a witness of the first arsenate detoxification
709 processes, since its appearance would have triggered additional stress to the communities (Chen
710 et al., 2017, 2020). The specific dynamics of the Dead Sea provides a setting to observe the
711 formation mechanisms for this kind of biosignature.

712 Geologically speaking, the potential for such a biosignature to be preserved in the geological
713 archives of the Earth can be complex. Examples from the Tumbiana stromatolites show potential
714 cell remnants and micro-pyrites tightly linked to ancient organic matter laminae bearing specific
715 As enrichments (Marin-Carbonne et al., 2018; Sforza et al., 2014), and well-preserved trace
716 metal-organic associations were indeed found in stromatolites and fossilized biofilms, such as
717 the Dresser Formation stromatolites (Baumgartner et al., 2020). However, this phenomenon of
718 exceptional organic matter preservation appears rare; modern examples of comparable sheet-like
719 microbial mats actively accreting in locations like Big Pond (Bahamas) or Hamelin Pool
720 (Western Australia) exhibit poor preservation of organic material, even at shallow depths (Glunk
721 et al., 2011; Sforza et al., 2016; Suosaari et al., 2022). In the microbial mat from the Dead Sea
722 pool presented here, rare CaCO₃ concretions found in the As-rich layer of the mat do not contain
723 As (Fig. 3). No sulfides are found either in these layers. Organic matter degradation could
724 possibly induce the precipitation of Fe-S minerals given how active the sulfur cycle is in the
725 Dead Sea environment (Häusler et al., 2014; Thomas et al., 2016). Produced sulfide should bind

726 As (Farquhar et al., 2002; Saunders et al., 2018) along with other trace metals like Cu, Pb, Cd
727 and Zn as shown by Moreau et al. (2013). As argued by Reid et al. (2024), the preservation
728 potential of microbial mats is primarily driven by the composition of the initial architecture
729 produced by the mat and the timing of lithification. Organic-rich mats, similar to the one
730 described in this study, contain localized precipitates drowned in organic matter (i.e. Sforza et
731 al., 2016). Taphonomic and/or diagenetic alteration of such organic-rich mats was inferred to
732 result in the formation of packstones or grainstones without obvious microbial contribution to
733 their formation (i.e., laminated fabrics, or preservation of cells; Reid et al., 2024). Consequently,
734 in the case of active microbialites in Big Pond, Bahamas, the preservation of metals (Cu, Zn, Fe,
735 and As) interpreted to be passively sorbed onto EPS (i.e., Sforza et al., 2016) may or may not be
736 preserved in the geological record. Thus, new insight from well-constrained modern microbialite
737 settings regarding the timing and mechanism of elemental enrichments and lithification is crucial
738 to accurate interpretation of the significance of ancient elemental enrichments in microbialites
739 throughout Earth history.

740 **5 Conclusions**

741 The observation of an As-rich microbial mat is the first of its kind in the Dead Sea environment
742 and provides the first evidence of high As concentrations in the vicinity of Dead Sea sinkholes
743 and freshwater springs near the inhabited area of Ein Gedi. Arsenic in the sinkhole and pond
744 water was effectively immobilized in the EPS of the microbial mats. The nature of the As in this
745 EPS has been interpreted as organoarsenic in minimally toxic forms, such as methylated
746 arsenate. Arsenic is not associated with mineral phases, so the fossilization potential of these
747 structures is probably poor, potentially allowing the remobilization of As upon degradation of the
748 mat. We suggest that the As concentration at specific levels in the mat is associated with pulses
749 of As contamination from spring water that have resulted in a detoxification response of the
750 communities present in the mat, through efflux and EPS binding . Therefore, this signature is not
751 linked to arsenotrophic processes carried out by microbial communities and is rather of
752 environmental origin, without providing information on energy-gaining metabolisms or on the
753 identity of the microbial population. We therefore urge caution in interpreting the As-rich
754 organic matter lamina in modern and ancient stromatolites and fossilized mat structures as
755 irrefutable evidence of arsenotrophy. Here, we showed that As enrichment may not be related to
756 a specific population signature, but rather to the confluence of variable environmental conditions
757 and the dynamic response of a microbial community well-adapted to extreme conditions. Given
758 the important role of the detoxification processes and sorption on EPS, high concentrations of As
759 in microbialites remain a fingerprint of life. However, it is important to recognize that As
760 enrichments in organic matter can inform us about energy-conserving As cycling microbes, but
761 can also provide information about chemical gradients or transient enrichments in early life
762 environments. The continued study of well-constrained, modern microbialite settings is therefore
763 critical to unraveling the impacts of environmental and microbial influences on the incorporation
764 of chemical biosignatures into microbial deposits that record the evolution of biogeochemical
765 cycles on Earth.

766 **Acknowledgments**

767 The authors thank Yaniv Darvasi for assistance and drone photography on the field, Serge Stoll
768 and Lina Ramirez for water analysis, and Iva Tomchovska for assistance in the lab. The AIFIRA
769 facility is financially supported by the CNRS, the University of Bordeaux and the Region
770 Nouvelle Aquitaine. We thank the technical staff members of the AIFIRA facility (J. Jouve) for
771 their help. This study was funded by the Swiss National Science Foundation project nr. 188571
772 (OASIS).

773

774 **Open Research**

775 All data and scripts used for this study and necessary for the reproduction of results are available
776 under the Open Science Framework Project available under the identifier DOI
777 10.17605/OSF.IO/X5F8B.

778 A preprint of this study has been submitted to EarthArXiv :

779

780 **References**

781 Abdel-Fattah, A., & Pingitore, N. E. (2009). Low levels of toxic elements in Dead Sea black mud and
782 mud-derived cosmetic products. *Environmental Geochemistry and Health*, 31(4), 487–492.
783 <https://doi.org/10.1007/s10653-008-9201-x>

784 Abdool-Ghany, A. A., Pollier, C. G. L., Oehlert, A. M., Swart, P. K., Blare, T., Moore, K., & Solo-
785 Gabriele, H. M. (2023). Assessing Quality and Beneficial Uses of Sargassum Compost. *SSRN*.

786 Abelson, M., Yechieli, Y., Baer, G., Lapid, G., Behar, N., Calvo, R., & Rosensaft, M. (2017). Natural
787 versus human control on subsurface salt dissolution and development of thousands of sinkholes
788 along the Dead Sea coast. *Journal of Geophysical Research: Earth Surface*, 122(6), 1262–1277.
789 <https://doi.org/10.1002/2017JF004219>

790 Abu Ghazleh, S., Hartmann, J., Jansen, N., & Kempe, S. (2009). Water input requirements of the rapidly
791 shrinking Dead Sea. *Naturwissenschaften*, 96(5), 637–643. [https://doi.org/10.1007/s00114-009-](https://doi.org/10.1007/s00114-009-0514-0)
792 0514-0

793 Adar, O., Groner, E., & Ben Natan, G. (2014). Colonization of a new habitat: The case of the Dead Sea
794 sinkholes-preliminary observations. *Dead Sea and Arava Studies*, 6(3), 89–74.

795 Ahsan, N., Faruque, K., Shamma, F., Islam, N., & Akhand, A. A. (2012). Arsenic adsorption by Bacterial
796 Extracellular Polymeric Substances. *Bangladesh Journal of Microbiology*, 28(2), 80–83.
797 <https://doi.org/10.3329/bjm.v28i2.11821>

798 Al-Halbouni, D., Watson, R. A., Holohan, E. P., Meyer, R., Polom, U., Dos Santos, F. M., et al. (2021).
799 Dynamics of hydrological and geomorphological processes in evaporite karst at the eastern Dead
800 Sea- A multidisciplinary study. *Hydrology and Earth System Sciences*, 25(6), 3351–3395.
801 <https://doi.org/10.5194/hess-25-3351-2021>

802 Anderson, G. L., Williams, J., & Hille, R. (1992). The purification and characterization of arsenite
803 oxidase from *Alcaligenes faecalis*, a molybdenum-containing hydroxylase. *Journal of Biological*
804 *Chemistry*, 267(33), 23674–23682. [https://doi.org/10.1016/s0021-9258\(18\)35891-5](https://doi.org/10.1016/s0021-9258(18)35891-5)

- 805 Andres, J., & Bertin, P. N. (2016). The microbial genomics of arsenic. *FEMS Microbiology Reviews*,
806 40(2), 299–322. <https://doi.org/10.1093/femsre/fuv050>
- 807 Arp, G., Reimer, A., & Reitner, J. (2003). Microbialite formation in seawater of increased alkalinity,
808 Satonda Crater Lake, Indonesia. *Journal of Sedimentary Research*, 73(1), 105. Retrieved from
809 <http://jsedres.geoscienceworld.org/cgi/content/abstract/73/1/105>
- 810 Bacquart, T., Devès, G., Carmona, A., Tucoulou, R., Bohic, S., & Ortega, R. (2007). Subcellular
811 speciation analysis of trace element oxidation states using synchrotron radiation micro-X-ray
812 absorption near-edge structure. *Analytical Chemistry*, 79(19), 7353–7359.
813 <https://doi.org/10.1021/ac0711135>
- 814 Bacquart, T., Devès, G., & Ortega, R. (2010). Direct speciation analysis of arsenic in sub-cellular
815 compartments using micro-X-ray absorption spectroscopy. *Environmental Research*, 110(5), 413–
816 416. <https://doi.org/10.1016/j.envres.2009.09.006>
- 817 Bankevich, A., Nurk, S., Antipov, D., Gurevich, A. A., Dvorkin, M., Kulikov, A. S., et al. (2012).
818 SPAdes: A New Genome Assembly Algorithm and Its Applications to Single-Cell Sequencing.
819 *Journal of Computational Biology*, 19(5), 455–477. <https://doi.org/10.1089/cmb.2012.0021>
- 820 Baumgartner, R. J., Van Kranendonk, M. J., Pagès, A., Fiorentini, M. L., Wacey, D., & Ryan, C. (2020).
821 Accumulation of transition metals and metalloids in sulfidized stromatolites of the 3.48 billion–
822 year–old Dresser Formation, Pilbara Craton. *Precambrian Research*, 337(April 2019), 105534.
823 <https://doi.org/10.1016/j.precamres.2019.105534>
- 824 Belmaker, R., Lazar, B., Stein, M., Taha, N., & Bookman, R. (2019). Constraints on aragonite
825 precipitation in the Dead Sea from geochemical measurements of flood plumes. *Quaternary Science*
826 *Reviews*, 221, 105876. <https://doi.org/10.1016/j.quascirev.2019.105876>
- 827 Bhattacharjee, H., & Rosen, B. P. (2007). Arsenic metabolism in prokaryotic and eukaryotic microbes. In
828 *Molecular microbiology of heavy metals* (pp. 371–406). Springer.
- 829 Bolger, A. M., Lohse, M., & Usadel, B. (2014). Trimmomatic: a flexible trimmer for Illumina sequence
830 data. *Bioinformatics*, 30(15), 2114–2120.
- 831 Bontognali, T. R. R., Vasconcelos, C., Warthmann, R. J., Bernasconi, S. M., Dupraz, C., Strohmenger, C.
832 J., & McKENZIE, J. a. (2010). Dolomite formation within microbial mats in the coastal sabkha of
833 Abu Dhabi (United Arab Emirates). *Sedimentology*, 57(3), 824–844. <https://doi.org/10.1111/j.1365-3091.2009.01121.x>
- 835 Butz, C., Grosjean, M., Fischer, D., Wunderle, S., Tylmann, W., & Rein, B. (2015). Hyperspectral
836 imaging spectroscopy: a promising method for the biogeochemical analysis of lake sediments.
837 *Journal of Applied Remote Sensing*, 9(1), 96031. <https://doi.org/10.1117/1.JRS.9.096031>
- 838 Butz, C., Grosjean, M., Goslar, T., & Tylmann, W. (2017). Hyperspectral imaging of sedimentary
839 bacterial pigments: a 1700-year history of meromixis from varved Lake Jaczno, northeast Poland.
840 *Journal of Paleolimnology*, 58(1), 57–72. <https://doi.org/10.1007/s10933-017-9955-1>
- 841 Callahan, B. J., McMurdie, P. J., Rosen, M. J., Han, A. W., Johnson, A. J. A., & Holmes, S. P. (2016).
842 DADA2: High-resolution sample inference from Illumina amplicon data. *Nature Methods*, 13(7),
843 581–583.
- 844 Campbell, J. L., Boyd, N. I., Grassi, N., Bonnicksen, P., & Maxwell, J. A. (2010). The Guelph PIXE
845 software package IV. *Nuclear Instruments and Methods in Physics Research Section B: Beam*
846 *Interactions with Materials and Atoms*, 268(20), 3356–3363.
847 <https://doi.org/https://doi.org/10.1016/j.nimb.2010.07.012>

- 848 Cantalapiedra, C. P., Huerta-cepas, J., Hern, A., Letunic, I., & Bork, P. (2021). eggNOG-mapper v2 :
849 Functional Annotation , Orthology Assignments, and Domain Prediction at the Metagenomic Scale.
850 *Molecular Biology and Evolution*, 38(12), 5825–5829. <https://doi.org/10.1093/molbev/msab293>
- 851 Caumette, G., Koch, I., & Reimer, K. J. (2012). Arsenobetaine formation in plankton: A review of studies
852 at the base of the aquatic food chain. *Journal of Environmental Monitoring*, 14(11), 2841–2853.
853 <https://doi.org/10.1039/c2em30572k>
- 854 Challenger, F. (1945). Biological methylation. *Chemical Reviews*, 36(3), 315–361.
855 <https://doi.org/10.1021/cr60115a003>
- 856 Chaumeil, P., Mussig, A. J., Parks, D. H., & Hugenholtz, P. (2020). Genome analysis GTDB-Tk : a
857 toolkit to classify genomes with the Genome Taxonomy Database. *Bioinformatics*, 36(November
858 2019), 1925–1927. <https://doi.org/10.1093/bioinformatics/btz848>
- 859 Chen, J., Bhattacharjee, H., & Rosen, B. P. (2015). ArsH is an organoarsenical oxidase that confers
860 resistance to trivalent forms of the herbicide monosodium methylarsenate and the poultry growth
861 promoter roxarsone. *Molecular Microbiology*, 96(5), 1042–1052.
862 <https://doi.org/10.1111/mmi.12988>
- 863 Chen, S. C., Sun, G. X., Rosen, B. P., Zhang, S. Y., Deng, Y., Zhu, B. K., et al. (2017). Recurrent
864 horizontal transfer of arsenite methyltransferase genes facilitated adaptation of life to arsenic.
865 *Scientific Reports*, 7(1), 1–11. <https://doi.org/10.1038/s41598-017-08313-2>
- 866 Chen, S. C., Sun, G. X., Yan, Y., Konstantinidis, K. T., Zhang, S. Y., Deng, Y., et al. (2020). The Great
867 Oxidation Event expanded the genetic repertoire of arsenic metabolism and cycling. *Proceedings of
868 the National Academy of Sciences of the United States of America*, 117(19), 10414–10421.
869 <https://doi.org/10.1073/pnas.2001063117>
- 870 Closson, D., & Abou Karaki, N. (2009). Human-induced geological hazards along the Dead Sea coast.
871 *Environmental Geology*, 58(2), 371–380. <https://doi.org/10.1007/s00254-008-1400-3>
- 872 Danecek, P., Bonfield, J. K., Liddle, J., Marshall, J., Ohan, V., Pollard, M. O., et al. (2021). Twelve years
873 of SAMtools and BCFtools. *Gigascience*, 10(2), giab008.
- 874 Deepika, K. V., Raghuram, M., Kariali, E., & Bramhachari, P. V. (2016). Biological responses of
875 symbiotic Rhizobium radiobacter strain VBCK1062 to the arsenic contaminated rhizosphere soils of
876 mung bean. *Ecotoxicology and Environmental Safety*, 134, 1–10.
877 <https://doi.org/10.1016/j.ecoenv.2016.08.008>
- 878 Delcher, A. L., Bratke, K. A., Powers, E. C., & Salzberg, S. L. (2007). Identifying bacterial genes and
879 endosymbiont DNA with Glimmer, 23(6), 673–679. <https://doi.org/10.1093/bioinformatics/btm009>
- 880 Duval, S., Ducluzeau, A. L., Nitschke, W., & Schoepp-Cothenet, B. (2008). Enzyme phylogenies as
881 markers for the oxidation state of the environment: The case of respiratory arsenate reductase and
882 related enzymes. *BMC Evolutionary Biology*, 8(1). <https://doi.org/10.1186/1471-2148-8-206>
- 883 Edmonds, J. S., Francesconi, K. A., Cannon, J. R., Raston, C. L., Skelton, B. W., & White, A. H. (1977).
884 Isolation, crystal structure and synthesis of arsenobetaine, the arsenical constituent of the western
885 rock lobster panulirus longipes cygnus George. *Tetrahedron Letters*, 18(18), 1543–1546.
886 [https://doi.org/https://doi.org/10.1016/S0040-4039\(01\)93098-9](https://doi.org/https://doi.org/10.1016/S0040-4039(01)93098-9)
- 887 Edwardson, C. F., & Hollibaugh, J. T. (2017). Metatranscriptomic analysis of prokaryotic communities
888 active in sulfur and arsenic cycling in Mono Lake, California, USA. *ISME Journal*, 11(10), 2195–
889 2208. <https://doi.org/10.1038/ismej.2017.80>

- 890 Eigenbrode, J. L., & Freeman, K. H. (2006). Late Archean rise of aerobic microbial ecosystems.
891 *Proceedings of the National Academy of Sciences of the United States of America*, 103(43), 15759–
892 15764. <https://doi.org/10.1073/pnas.0607540103>
- 893 Farías, M. E., Rascovan, N., Toneatti, D. M., Albarracín, V. H., Flores, M. R., Poiré, D. G., et al. (2013).
894 The Discovery of Stromatolites Developing at 3570 m above Sea Level in a High-Altitude Volcanic
895 Lake Socompa, Argentinean Andes. *PLoS ONE*, 8(1). <https://doi.org/10.1371/journal.pone.0053497>
- 896 Farquhar, M. L., Charnock, J. M., Livens, F. R., & Vaughan, D. J. (2002). Mechanisms of arsenic uptake
897 from aqueous solution by interaction with goethite, lepidocrocite, mackinawite, and pyrite: An X-
898 ray absorption spectroscopy study. *Environmental Science and Technology*, 36(8), 1757–1762.
899 <https://doi.org/10.1021/es010216g>
- 900 Fernandez, A. B., Rasuk, M. C., Visscher, P. T., Contreras, M., Novoa, F., Poire, D. G., et al. (2016).
901 Microbial diversity in sediment ecosystems (evaporites domes, microbial mats, and crusts) of
902 Hypersaline Laguna Tebenquiche, Salar de Atacama, Chile. *Frontiers in Microbiology*, 7(AUG), 1–
903 18. <https://doi.org/10.3389/fmicb.2016.01284>
- 904 Filella, M., Wey, S., Matoušek, T., Coster, M., Rodríguez-Murillo, J. C., & Loizeau, J. L. (2023). Arsenic
905 in Lake Geneva (Switzerland, France): long term monitoring, and redox and methylation speciation
906 in an As unpolluted, oligo-mesotrophic lake. *Environmental Science: Processes and Impacts*, 25(4),
907 850–869. <https://doi.org/10.1039/d2em00431c>
- 908 Glunk, C., Dupraz, C., Braissant, O., Gallagher, K. L., Verrecchia, E. P., Visscher, P. T., et al. (2011).
909 Microbially mediated carbonate precipitation in a hypersaline lake, Big Pond (Eleuthera, Bahamas).
910 *Sedimentology*, 58(3), 720–736. <https://doi.org/10.1111/j.1365-3091.2010.01180.x>
- 911 Häusler, S., Noriega-Ortega, B. E., Polerecky, L., Meyer, V., de Beer, D., & Ionescu, D. (2014).
912 Microenvironments of reduced salinity harbour biofilms in Dead Sea underwater springs.
913 *Environmental Microbiology Reports*, 6(2), 152–8. <https://doi.org/10.1111/1758-2229.12140>
- 914 Häusler, S., Weber, M., Siebert, C., Holtappels, M., Noriega-Ortega, B. E., De Beer, D., & Ionescu, D.
915 (2014). Sulfate reduction and sulfide oxidation in extremely steep salinity gradients formed by
916 freshwater springs emerging into the Dead Sea. *FEMS Microbiology Ecology*, 90(3), 956–69.
917 <https://doi.org/10.1111/1574-6941.12449>
- 918 Herbel, M. J., Switzer Blum, J., Hoefft, S. E., Cohen, S. M., Arnold, L. L., Lisak, J., et al. (2002).
919 Dissimilatory arsenate reductase activity and arsenate-respiring bacteria in bovine rumen fluid,
920 hamster feces, and the termite hindgut. *FEMS Microbiology Ecology*, 41(1), 59–67.
921 [https://doi.org/10.1016/S0168-6496\(02\)00266-0](https://doi.org/10.1016/S0168-6496(02)00266-0)
- 922 Hirshberg, O., & Ben-Ami, F. (2019). Sinkholes as a source of life in the Dead Sea region. *Aquatic
923 Sciences*, 0(0), 0. <https://doi.org/10.1007/s00027-018-0611-2>
- 924 Honschopp, S., Brunken, N., Nehrkorn, A., & Breunig, H. J. (1996). Isolation and characterization of a
925 new arsenic methylating bacterium from soil. *Microbiological Research*, 151(1), 37–41.
926 [https://doi.org/10.1016/S0944-5013\(96\)80053-X](https://doi.org/10.1016/S0944-5013(96)80053-X)
- 927 Ionescu, D., Siebert, C., Polerecky, L., Munwes, Y. Y., Lott, C., Häusler, S., et al. (2012). Microbial and
928 chemical characterization of underwater fresh water springs in the Dead Sea. *PloS One*, 7(6),
929 e38319. <https://doi.org/10.1371/journal.pone.0038319>
- 930 Jahrman, E. P., Yu, L. L., Krekelberg, W. P., Sheen, D. A., Allison, T. C., & Molloy, J. L. (2022).
931 Assessing arsenic species in foods using regularized linear regression of the arsenic K-edge X-ray
932 absorption near edge structure. *Journal of Analytical Atomic Spectrometry*, 37(6), 1247–1258.

- 933 <https://doi.org/10.1039/d1ja00445j>
- 934 Kanehisa, M., Sato, Y., & Morishima, K. (2016). BlastKOALA and GhostKOALA : KEGG Tools for
935 Functional Characterization of Genome and Metagenome Sequences. *Journal of Molecular Biology*,
936 428(4), 726–731. <https://doi.org/10.1016/j.jmb.2015.11.006>
- 937 Kang, D. D., Froula, J., Egan, R., & Wang, Z. (2015). MetaBAT, an efficient tool for accurately
938 reconstructing single genomes from complex microbial communities. *PeerJ*, 1–15.
939 <https://doi.org/10.7717/peerj.1165>
- 940 Kazmierczak, J., & Kempe, S. (2003). Modern terrestrial analogues for the carbonate globules in Martian
941 meteorite ALH84001. *Naturwissenschaften*, (90), 167–172. [https://doi.org/10.1007/s00114-003-](https://doi.org/10.1007/s00114-003-0411-x)
942 0411-x
- 943 Kempe, S., Kremer, B., Moreira, D., & Tavera, R. (2011). Hydrochemistry and microbialites of the
944 alkaline crater lake Alchichica, Mexico. *Facies*, (57), 543–570. [https://doi.org/10.1007/s10347-010-](https://doi.org/10.1007/s10347-010-0255-8)
945 0255-8
- 946 Kotova, I., Kayukova, E., & Kotov, S. (2016). Peloids of Crimean salt lakes and the Dead Sea: controls
947 on composition and formation. *Environmental Earth Sciences*, 75(16), 1–14.
948 <https://doi.org/10.1007/s12665-016-5999-1>
- 949 Kulp, T. R., Hoefft, S. E., Asao, M., Madigan, M. T., Hollibaugh, J. T., Fisher, J. C., et al. (2008).
950 Arsenic(III) Fuels Anoxygenic Photosynthesis in Hot Spring Biofilms from Mono Lake, California.
951 *Science*, 321, 967–970.
- 952 Lakso, J. U., & Peoples, S. A. (1975). Methylation of Inorganic Arsenic by Mammals. *Journal of*
953 *Agricultural and Food Chemistry*, 23(4), 674–676. <https://doi.org/10.1021/jf60200a028>
- 954 Lebrun, E., Brugna, M., Baymann, F., Muller, D., Lièvreumont, D., Lett, M. C., & Nitschke, W. (2003).
955 Arsenite oxidase, an ancient bioenergetic enzyme. *Molecular Biology and Evolution*, 20(5), 686–
956 693. <https://doi.org/10.1093/molbev/msg071>
- 957 Lensky, N. G., Dvorkin, Y., Lyakhovsky, V., Gertman, I., & Gavrieli, I. (2005). Water, salt, and energy
958 balances of the Dead Sea. *Water Resources Research*, 41(12), 1–13.
959 <https://doi.org/10.1029/2005WR004084>
- 960 Levy, E. J., Thomas, C., Antler, G., Gavrieli, I., Turchyn, A. V., Grossi, V., et al. (2022). Intensified
961 microbial sulfate reduction in the deep Dead Sea during the early Holocene Mediterranean sapropel
962 1 deposition. *Geobiology*, 1–15.
- 963 Luvonga, C., Rimmer, C. A., Yu, L. L., & Lee, S. B. (2020). Organoarsenicals in Seafood: Occurrence,
964 Dietary Exposure, Toxicity, and Risk Assessment Considerations - A Review. *Journal of*
965 *Agricultural and Food Chemistry*, 68(4), 943–960. <https://doi.org/10.1021/acs.jafc.9b07532>
- 966 Marin-Carbonne, J., Remusat, L., Sforza, M. C., Thomazo, C., Cartigny, P., & Philippot, P. (2018).
967 Sulfur isotope's signal of nanopyrates enclosed in 2.7 Ga stromatolitic organic remains reveal
968 microbial sulfate reduction. *Geobiology*, 16(2), 121–138. <https://doi.org/10.1111/gbi.12275>
- 969 Martin, M. (2011). Cutadapt removes adapter sequences from high-throughput sequencing reads.
970 *EMBnet. Journal*, 17(1), 10–12.
- 971 McBride, B. C., & Wolfe, R. S. (1971). Biosynthesis of Dimethylarsine by Methanobacterium.
972 *Biochemistry*, 10(23), 4312–4317. <https://doi.org/10.1021/bi00799a024>
- 973 McEwan, A. G., Ridge, J. P., McDevitt, C. A., & Hugenholtz, P. (2002). The DMSO reductase family of

- 974 microbial molybdenum enzymes; molecular properties and role in the dissimilatory reduction of
975 toxic elements. *Geomicrobiology Journal*, 19(1), 3–21.
976 <https://doi.org/10.1080/014904502317246138>
- 977 McMurdie, P. J., & Holmes, S. (2013). Phyloseq: An R Package for Reproducible Interactive Analysis
978 and Graphics of Microbiome Census Data. *PLoS ONE*, 8(4).
979 <https://doi.org/10.1371/journal.pone.0061217>
- 980 Moller, P., Rosenthal, E., Geyer, S., Guttman, J., Dulski, P., Rybakov, M., et al. (2007). Hydrochemical
981 processes in the lower Jordan valley and in the Dead Sea area. *Chemical Geology*, 239(1–2), 27–49.
982 <https://doi.org/10.1016/j.chemgeo.2006.12.004>
- 983 Moreau, J. W., Fournelle, J. H., & Banfield, J. F. (2013). Quantifying heavy metals sequestration by
984 sulfate-reducing bacteria in an acid mine drainage-contaminated natural wetland. *Frontiers in*
985 *Microbiology*, 4(MAR), 1–10. <https://doi.org/10.3389/fmicb.2013.00043>
- 986 Morita, M., & Shibata, Y. (1990). Chemical form of arsenic in marine macroalgae. *Applied*
987 *Organometallic Chemistry*, 4(3), 181–190. <https://doi.org/10.1002/aoc.590040303>
- 988 Mukhopadhyay, R., Rosen, B. P., Phung, L. T., & Silver, S. (2002). Microbial arsenic: From geocycles to
989 genes and enzymes. *FEMS Microbiology Reviews*, 26(3), 311–325. [https://doi.org/10.1016/S0168-](https://doi.org/10.1016/S0168-6445(02)00112-2)
990 [6445\(02\)00112-2](https://doi.org/10.1016/S0168-6445(02)00112-2)
- 991 Naveed, S., Li, C., Lu, X., Chen, S., Yin, B., Zhang, C., & Ge, Y. (2019). Microalgal extracellular
992 polymeric substances and their interactions with metal(loid)s: A review. *Critical Reviews in*
993 *Environmental Science and Technology*, 49(19), 1769–1802.
994 <https://doi.org/10.1080/10643389.2019.1583052>
- 995 Naveed, S., Li, C., Zhang, J., Zhang, C., & Ge, Y. (2020). Sorption and transformation of arsenic by
996 extracellular polymeric substances extracted from *Synechocystis* sp. PCC6803. *Ecotoxicology and*
997 *Environmental Safety*, 206(September), 111200. <https://doi.org/10.1016/j.ecoenv.2020.111200>
- 998 Nissenbaum, A. (1977). Minor and trace elements in Dead Sea water. *Chemical Geology*, 19(1–4), 99–
999 111. [https://doi.org/10.1016/0009-2541\(77\)90008-0](https://doi.org/10.1016/0009-2541(77)90008-0)
- 1000 Nof, R. N., Abelson, M., Raz, E., Magen, Y., Atzori, S., Salvi, S., & Baer, G. (2019). SAR Interferometry
1001 for Sinkhole Early Warning and Susceptibility Assessment along the Dead Sea, Israel. *Remote*
1002 *Sensing*, (Figure 1), 5–20. <https://doi.org/10.3390/rs11010089>
- 1003 Oksanen, J., Kindt, R., Legendre, P., O'Hara, B., Stevens, M. H. H., Oksanen, M. J., & Suggests, M.
1004 (2007). The vegan package. *Community Ecology Package*, 10.
- 1005 Oremland, R., & Stolz, J. (2003). The Ecology of Arsenic. *Science*, 300(May), 939–944.
- 1006 Oremland, R. S., Kulp, T. R., Blum, J. S., Hoelt, S. E., Baesman, S., Miller, L. G., & Stolz, J. F. (2005).
1007 Microbiology: A microbial arsenic cycle in a salt-saturated, extreme environment. *Science*,
1008 308(5726), 1305–1308. <https://doi.org/10.1126/science.1110832>
- 1009 Oremland, R. S., Saltikov, C. W., Wolfe-Simon, F., & Stolz, J. F. (2009). Arsenic in the evolution of
1010 earth and extraterrestrial ecosystems. *Geomicrobiology Journal*, 26(7), 522–536.
1011 <https://doi.org/10.1080/01490450903102525>
- 1012 Oremland, R. S., Saltikov, C. W., Stolz, J. F., & Hollibaugh, J. T. (2017). Autotrophic microbial
1013 arsenotrophy in arsenic-rich soda lakes. *FEMS Microbiology Letters*, 364(15).
1014 <https://doi.org/10.1093/femsle/fnx146>

- 1015 Oren, A. (1993). The Dead Sea—alive again. *Cellular and Molecular Life Sciences*, 49(6), 518–522.
- 1016 Oren, A, Gurevich, P., Anati, D., Barkan, E., & Luz, B. (1995). A bloom of *Dunaliella parva* in the Dead
1017 Sea in 1992: biological and biogeochemical aspects. *Hydrobiologia*, 297(297), 173–185.
- 1018 Oren, Aharon. (1983). Population dynamics of halobacteria in the Dead Sea water column. *Limnology
1019 and Oceanography*, 28(6), 1094–1103.
- 1020 Oren, Aharon. (1999). Microbiological studies in the Dead Sea: Future challenges toward the
1021 understanding of life at the limit of salt concentrations. *Hydrobiologia*, 405, 1–9.
1022 <https://doi.org/10.1023/A:1003879932328>
- 1023 Oren, Aharon. (2010). The dying Dead Sea: The microbiology of an increasingly extreme environment.
1024 *Lakes & Reservoirs: Research & Management*, 15(3), 215–222. [https://doi.org/10.1111/j.1440-
1025 1770.2010.00435.x](https://doi.org/10.1111/j.1440-1770.2010.00435.x)
- 1026 Pace, A., Bourillot, R., Bouton, A., Vennin, E., Braissant, O., Dupraz, C., et al. (2018). Formation of
1027 stromatolite lamina at the interface of oxygenic-anoxygenic photosynthesis. *Geobiology*, (February),
1028 378–398. <https://doi.org/10.1111/gbi.12281>
- 1029 Parks, D. H., Imelfort, M., Skennerton, C. T., Hugenholtz, P., & Tyson, G. W. (2015). CheckM :
1030 assessing the quality of microbial genomes recovered from isolates , single cells , and metagenomes.
1031 *Genome Research*, 1043–1055. <https://doi.org/10.1101/gr.186072.114>.Freely
- 1032 Qin, J., Rosen, B. P., Zhang, Y., Wang, G., Franke, S., & Rensing, C. (2006). Arsenic detoxification and
1033 evolution of trimethylarsine gas by a microbial arsenite S-adenosylmethionine methyltransferase.
1034 *Proceedings of the National Academy of Sciences of the United States of America*, 103(7), 2075–
1035 2080. <https://doi.org/10.1073/pnas.0506836103>
- 1036 Reid, R. P., Suosaari, E. P., Oehlert, A. M., Pollier, C. G. L., & Dupraz, C. (2024). Microbialite Accretion
1037 and Growth : Lessons from Shark Bay and the Bahamas, 1–25.
- 1038 Rein, B., & Sirocko, F. (2002). In-situ reflectance spectroscopy - Analysing techniques for high-
1039 resolution pigment logging in sediment cores. *International Journal of Earth Sciences*, 91(5), 950–
1040 954. <https://doi.org/10.1007/s00531-002-0264-0>
- 1041 Rosen, B. P. (2002). Biochemistry of arsenic detoxification. *FEBS Letters*, 529, 86–92. Retrieved from
1042 [http://linkinghub.elsevier.com/retrieve/pii/S0014579302031861%5Cnpapers2://publication/uuid/AA
1043 429994-D6E2-4D6F-852E-62D148F55C7D](http://linkinghub.elsevier.com/retrieve/pii/S0014579302031861%5Cnpapers2://publication/uuid/AA429994-D6E2-4D6F-852E-62D148F55C7D)
- 1044 Saikat, S. Q., Selim, A. M., Kessi, J., Wehrli, E., & Hanselmann, K. W. (2001). Transformation of arsenic
1045 compounds by bacteria from groundwater sediments of Bangladesh. Technical report.
- 1046 Sancho-Tomás, M., Somogyi, A., Medjoubi, K., Bergamaschi, A., Visscher, P. T., Van Driessche, A. E.
1047 S., et al. (2018). Distribution, redox state and (bio)geochemical implications of arsenic in present
1048 day microbialites of Laguna Brava, Salar de Atacama. *Chemical Geology*, 490(7), 13–21.
1049 <https://doi.org/10.1016/j.chemgeo.2018.04.029>
- 1050 Saona, L. A., Soria, M., Durán-Toro, V., Wörmer, L., Milucka, J., Castro-Nallar, E., et al. (2021).
1051 Phosphate-Arsenic Interactions in Halophilic Microorganisms of the Microbial Mat from Laguna
1052 Tebenquiche: from the Microenvironment to the Genomes. *Microbial Ecology*, 81(4), 941–953.
1053 <https://doi.org/10.1007/s00248-020-01673-9>
- 1054 Saunders, J. A., Lee, M. K., Dhakal, P., Ghandehari, S. S., Wilson, T., Billor, M. Z., & Uddin, A. (2018).
1055 Bioremediation of arsenic-contaminated groundwater by sequestration of arsenic in biogenic pyrite.
1056 *Applied Geochemistry*, 96(November 2017), 233–243.

- 1057 <https://doi.org/10.1016/j.apgeochem.2018.07.007>
- 1058 Schmidt, L., Landero, J. A., Novo, D. L. R., Duarte, F. A., Mesko, M. F., Caruso, J. A., & Flores, E. M.
1059 M. (2018). A feasible method for As speciation in several types of seafood by LC-ICP-MS/MS.
1060 *Food Chemistry*, 255(September 2017), 340–347. <https://doi.org/10.1016/j.foodchem.2018.02.079>
- 1061 Schoepp-Cothenet, B., Duval, S., Santini, J. M., & Nitschke, W. (2009). Comment on “Arsenic (III) fuels
1062 anoxygenic photosynthesis in hot spring biofilms from Mono Lake, California.” *Science*, 323(5914).
1063 <https://doi.org/10.1126/science.1164967>
- 1064 Seemann, T. (2014). Prokka : rapid prokaryotic genome annotation. *Bioinformatics*, 30(14), 2068–2069.
1065 <https://doi.org/10.1093/bioinformatics/btu153>
- 1066 Sforina, M. C., Daye, M., Philippot, P., Somogyi, A., van Zuilen, M. A., Medjoubi, K., et al. (2016).
1067 Patterns of metal distribution in hypersaline microbialites during early diagenesis: Implications for
1068 the fossil record. *Geobiology*, 15(2), 259–279. <https://doi.org/10.1111/gbi.12218>
- 1069 Sforina, Marie Catherine, Philippot, P., Somogyi, A., Van Zuilen, M. A., Medjoubi, K., Schoepp-
1070 Cothenet, B., et al. (2014). Evidence for arsenic metabolism and cycling by microorganisms 2.7
1071 billion years ago. *Nature Geoscience*, 7(11), 811–815. <https://doi.org/10.1038/ngeo2276>
- 1072 Shalev, E., Lyakhovskiy, V., & Yechieli, Y. (2006). Salt dissolution and sinkhole formation along the
1073 Dead Sea shore. *Journal of Geophysical Research: Solid Earth*, 111(3), 1–12.
1074 <https://doi.org/10.1029/2005JB004038>
- 1075 Sidle, W. C., Wotten, B., & Murphy, E. (2001). Provenance of geogenic arsenic in the Goose River basin,
1076 Maine, USA. *Environmental Geology*, 41.
- 1077 Singh, M., Pandey, S., Kumar, A., & Pandey, K. D. (2021). *Microbial biofilms for the remediation of*
1078 *contaminated water. Microbe Mediated Remediation of Environmental Contaminants*. INC.
1079 <https://doi.org/10.1016/b978-0-12-821199-1.00021-3>
- 1080 Smith, P. G., Koch, I., Gordon, R. A., Mandoli, D. F., Chapman, B. D., & Reimer, K. J. (2005). X-ray
1081 absorption near-edge structure analysis of arsenic species for application to biological environmental
1082 samples. *Environmental Science and Technology*, 39(1), 248–254.
1083 <https://doi.org/10.1021/es049358b>
- 1084 Solé, V. A., Papillon, E., Cotte, M., Walter, P., & Susini, J. (2007). A multiplatform code for the analysis
1085 of energy-dispersive X-ray fluorescence spectra. *Spectrochimica Acta Part B: Atomic Spectroscopy*,
1086 62(1), 63–68. <https://doi.org/https://doi.org/10.1016/j.sab.2006.12.002>
- 1087 Sorrel, P., Jacq, K., Van Exem, A., Escarguel, G., Dietre, B., Debret, M., et al. (2021). Evidence for
1088 centennial-scale Mid-Holocene episodes of hypolimnetic anoxia in a high-altitude lake system from
1089 central Tian Shan (Kyrgyzstan). *Quaternary Science Reviews*, 252.
1090 <https://doi.org/10.1016/j.quascirev.2020.106748>
- 1091 Stüeken, E. E., Buick, R., Anderson, R. E., Baross, J. A., Planavsky, N. J., & Lyons, T. W. (2017).
1092 Environmental niches and metabolic diversity in Neoproterozoic lakes. *Geobiology*, 15(6), 767–783.
1093 <https://doi.org/10.1111/gbi.12251>
- 1094 Suosaari, E. P., Lascu, I., Oehlert, A. M., Parlanti, P., Mugnaioli, E., Gemmi, M., et al. (2022).
1095 Authigenic clays as precursors to carbonate precipitation in saline lakes of Salar de Llamara,
1096 Northern Chile. *Communications Earth and Environment*, 3(1), 1–12.
1097 <https://doi.org/10.1038/s43247-022-00658-5>
- 1098 Suosaari, E. P., Reid, R. P., Mercadier, C., Vitek, B. E., Oehlert, A. M., Stolz, J. F., et al. (2022). The

- 1099 microbial carbonate factory of Hamelin Pool, Shark Bay, Western Australia. *Scientific Reports*,
1100 12(1), 1–12. <https://doi.org/10.1038/s41598-022-16651-z>
- 1101 Switzer, J., Allana, B., Bindi, B., Buzzelli, J., Stolz, J. F., & Oremland, R. S. (1998). *Bacillus*
1102 *arsenicosenenatis*, sp. nov., and *Bacillus selenitireducens*, sp. nov. : two haloalkaliphiles from Mono
1103 Lake, California that respire oxyanions of selenium and arsenic. *Archives of Microbiology*, 171, 19–
1104 30.
- 1105 Switzer, J., John, B., Aharon, F. S., & Oremland, R. S. (2001). *Selenihalanaerobacter shriftii* gen. nov.,
1106 sp. nov., a halophilic anaerobe from Dead Sea sediments that respire selenate. *Archives of*
1107 *Microbiology*, 175, 208–219.
- 1108 Team, R. C. (2013). R: A language and environment for statistical computing.
- 1109 Thomas, C., Ionescu, D., Ariztegui, D., & Party, the D. S. (2014). Archaeal populations in two distinct
1110 sedimentary facies of the subsurface of the Dead Sea. *Marine Genomics*, 17, 53–62.
1111 <https://doi.org/10.1016/j.margen.2014.09.001>
- 1112 Thomas, C., Ebert, Y., Kiro, Y., Stein, M., & Ariztegui, D. (2016). Microbial sedimentary imprint on the
1113 deep Dead Sea sediment. *The Depositional Record*, 1–21. <https://doi.org/10.1002/dep2.16>
- 1114 Thomas, C., Gedulter, N., Darvasi, Y., Bundeleva, I. A., Torfstein, A., Agnon, A., & Ariztegui, D.
1115 (2021). Arsenic enrichment and organomineralizations in microbial mats of the Dead Sea shores. In
1116 *Goldschmidt 2021 Meeting abstracts*.
- 1117 Thomazo, C., Ader, M., & Philippot, P. (2011). Extreme 15N-enrichments in 2.72-Gyr-old sediments:
1118 Evidence for a turning point in the nitrogen cycle. *Geobiology*, 9(2), 107–120.
1119 <https://doi.org/10.1111/j.1472-4669.2011.00271.x>
- 1120 Visscher, P. T., Gallagher, K. L., Bouton, A., Farias, M. E., Kurth, D., Sancho-Tomás, M., et al. (2020).
1121 Modern arsenotrophic microbial mats provide an analogue for life in the anoxic Archean.
1122 *Communications Earth & Environment*, 1(1), 1–10. <https://doi.org/10.1038/s43247-020-00025-2>
- 1123 Wang, Ya, Wang, S., Xu, P., Liu, C., Liu, M., Wang, Y., et al. (2015). Review of arsenic speciation,
1124 toxicity and metabolism in microalgae. *Reviews in Environmental Science and Biotechnology*,
1125 14(3), 427–451. <https://doi.org/10.1007/s11157-015-9371-9>
- 1126 Wang, Yong, & Qian, P. Y. (2009). Conservative fragments in bacterial 16S rRNA genes and primer
1127 design for 16S ribosomal DNA amplicons in metagenomic studies. *PLoS ONE*, 4(10).
1128 <https://doi.org/10.1371/journal.pone.0007401>
- 1129 Wong, H. L., Smith, D.-L., Visscher, P. T., & Burns, B. P. (2015). Niche differentiation of bacterial
1130 communities at a millimeter scale in Shark Bay microbial mats. *Scientific Reports*, 5(November),
1131 15607. <https://doi.org/10.1038/srep15607>
- 1132 Wu, Y., Kukkadapu, R. K., Livi, K. J. T., Xu, W., Li, W., & Sparks, D. L. (2018). Iron and Arsenic
1133 Speciation during As(III) Oxidation by Manganese Oxides in the Presence of Fe(II): Molecular-
1134 Level Characterization Using XAFS, Mössbauer, and TEM Analysis. *ACS Earth and Space*
1135 *Chemistry*, 2(3), 256–268. <https://doi.org/10.1021/acsearthspacechem.7b00119>
- 1136 Xu, C., Zhou, T., Kuroda, M., & Rosen, B. P. (1998). Metalloid resistance mechanisms in prokaryotes.
1137 *Journal of Biochemistry*, 123(1), 16–23. <https://doi.org/10.1093/oxfordjournals.jbchem.a021904>
- 1138 Yan, P., Xia, J. S., Chen, Y. P., Liu, Z. P., Guo, J. S., Shen, Y., et al. (2017). Thermodynamics of binding
1139 interactions between extracellular polymeric substances and heavy metals by isothermal titration
1140 microcalorimetry. *Bioresource Technology*, 232, 354–363.

- 1141 <https://doi.org/10.1016/j.biortech.2017.02.067>
- 1142 Yang, H. C., & Rosen, B. P. (2016). New mechanisms of bacterial arsenic resistance. *Biomedical Journal*,
1143 39(1), 5–13. <https://doi.org/10.1016/j.bj.2015.08.003>
- 1144 Yechieli, Y., Abelson, M., Bein, A., Crouvi, O., & Shtivelman, V. (2006). Sinkhole “swarms” along the
1145 Dead Sea coast: Reflection of disturbance of lake and adjacent groundwater systems. *Bulletin of the*
1146 *Geological Society of America*, 118(9–10), 1075–1087. <https://doi.org/10.1130/B25880.1>
- 1147 Zander, P. D., Wienhues, G., & Grosjean, M. (2022). Scanning Hyperspectral Imaging for In Situ
1148 Biogeochemical Analysis of Lake Sediment Cores: Review of Recent Developments. *Journal of*
1149 *Imaging*, 8(3). <https://doi.org/10.3390/jimaging8030058>
- 1150 Zargar, K., Hoef, S., Oremland, R., & Saltikov, C. W. (2010). Identification of a novel arsenite oxidase
1151 gene, *arxA*, in the haloalkaliphilic, arsenite-oxidizing bacterium *Alkalilimnicola ehrlichii* strain
1152 MLHE-1. *Journal of Bacteriology*, 192(14), 3755–3762. <https://doi.org/10.1128/JB.00244-10>
- 1153 Zeyen, N., Benzerara, K., Li, J., Groleau, A., Balan, E., Robert, J. L., et al. (2015). Formation of low-T
1154 hydrated silicates in modern microbialites from Mexico and implications for microbial fossilization.
1155 *Frontiers in Earth Science*, 3(October), 1–23. <https://doi.org/10.3389/feart.2015.00064>
- 1156 Zhu, Y. G., Yoshinaga, M., Zhao, F. J., & Rosen, B. P. (2014). Earth abides arsenic biotransformations.
1157 *Annual Review of Earth and Planetary Sciences*, 42, 443–467. [https://doi.org/10.1146/annurev-](https://doi.org/10.1146/annurev-earth-060313-054942)
1158 [earth-060313-054942](https://doi.org/10.1146/annurev-earth-060313-054942)
- 1159 Zilberman, T., Gavrieli, I., Yechieli, Y., Gertman, I., & Katz, A. (2017). 1. Constraints on evaporation
1160 and dilution of terminal, hypersaline lakes under negative water balance: the Dead Sea, Israel.
1161 *Geochimica et Cosmochimica Acta*. <https://doi.org/10.1016/j.gca.2017.08.040>

1162

1163 Supporting Information

1164 Fig. S1: Photographs of occurrence of diatoms, filamentous organisms and coccoid organisms
1165 and aragonite precipitates in the mat sample (pool 1). (A) Autofluorescence photograph of a
1166 region of the As-rich layer, seen under DAPI filter (no staining). The forms of diatoms can be
1167 observed throughout the samples and examples are pointed by the black arrows.
1168 B/Autofluorescence photograph of the same region seen under combined APC and Rhodamine
1169 filter (no staining; filter for APC: red color covering autofluorescence of chlorophyll,
1170 allophycocyanin and phycocyanin; filter for Rhodamine: yellow color covering autofluorescence
1171 of cyanobacterial phycoerythrin and phycoerythrocyanin). Filaments appear clearly throughout
1172 the sample, along with numerous coccoidal and rod-shaped microorganisms, with dominance of
1173 red suggesting the presence of a large number of photosynthetic or chlorophyll-pigmented
1174 organisms. C/ Scanning electron microscope image of a diatoms lying on EPS of the microbial
1175 mat from pool 1. A large number of coccoid cells are observed associated with filaments formed
1176 by the microbial mat. Some small detrital minerals (clay minerals) and aragonite needles can be
1177 observed too. D/ Scanning electron microscope photograph of the polished resin sample from
1178 pool 1 under back-scattered electron mode. The white minerals are aragonite needles
1179 progressively agglomerating into larger aragonite concretions. A later stage aragonite concretion
1180 is seen right below the needle agglomerates. Darker grey colors within the concretion and
1181 aragonite needle accumulation report an increased presence of Mg-Si within the Ca-dominated
1182 minerals. E/ Autofluorescence photograph under DAPI filter of the same aragonite agglomerate

1183 and concretions. Aragonite is seen in autofluorescent light blue, within a darker blue matrix of
1184 EPS mixed with resin.

1185 Fig. S2: (top) spectral profile of the sample with prominent absorption trough at 550nm, 620nm,
1186 660nm, and 915nm. (bottom spectral profile of the embedding resin with prominent absorption
1187 troughs at 560-570nm, 630nm, 710nm, 820nm, 870nm and 915nm. X-axis shows wavelengths
1188 and y-axis show absorbance, where 1 is no absorbance.

1189 Fig. S3: Summary plots and spatial distribution of detected pigments: RABD612 stands for
1190 cyanobacteria pigment phycocyanin, RABD660 represents chlorophyll-a and its green
1191 derivatives. RABD715 should show bacteriochlorophyll-c, d and e and RABD820 show the resin
1192 signal. Index values above 1 are showing the absorbance at given wavelength.

1193 Fig. S4: PIXE spectra showing identified peaks within the As-rich lamina of the mat of pool 1.

1194 Fig. S5: Redox maps at the As K-edge : 11850eV, 11868 eV, 11873 eV, 11880 eV, 11890 eV for
1195 regions 1 to 4 of the microbial mat of pool 1 (shown in Figure 3 of the main text), and
1196 corresponding XANES profiles for all regions/points analysed.

1197